جامعة الموصل
كلية الهندسة

دراسة وتنفيذ كاشف ضوئي للأشعة تحت الحمراء باستخدام السيليكون المطعم بالانديوم

عمر بدر محمد خضر

رسالة ماجستير
هندسة كهرباء / الكترونيك واتصالات /
(الحالة الصلبة)

بإشراف
الأستاذ المساعد
الدكتور خالد خليل محمد

1432 هـ
2010 م

جامعة الموصل
كلية الهندسة

دراسة وتنفيذ كاشف ضوئي للأشعة تحت الحمراء باستخدام السيليكون المطعم بالانديوم

رسالة تقدم بها

عمر بدر محمد خضر

الى

مجلس كلية الهندسة في جامعة الموصل

وهي جزء من متطلبات نيل شهادة الماجستير

علوم في الهندسة الكهربائية/الكترونيك واتصالات/

(الحالة الصلبة)

بإشراف

الأستاذ المساعد

الدكتور خالد خليل محمد

1432 هـ
2010 م

الخلاصة

في هذا العمل تمت دراسة وتنفيذ كاشف أشعة تحت الحمراء باستخدام خلايا سيليكونية مع مادة الانديوم, حيث ان تطعيم السيليكون بمادة الانديوم يؤثر على خواص الاستجابة الطيفية للكاشف المصنَع وذلك بسبب الدور الذي يقوم به الانديوم كمركز تولد– اعادة اتحاد.

وللحصول على النماذج الحاسوبية للكواشف تحت الدراسة, تم استخدام برنامج المحاكاة الحاسوبي (SCAPS) وذلك لغرض دراسة وتحليل عمل هذه الكواشف. حيث يستخدم برنامج المحاكاة (SCAPS) لدراسة وتحليل نبائط أشباه الموصلات بشكل عام.

وللحصول على الكواشف التي تمت دراسة وتحليل خواصها حاسوبيا, بشكل عملي تم استخدام طريقة التبخير الفراغية بواسطة منظومة التبخير الفراغية Balzers BA 510 , كما وتمت دراسة تأثير الأجراءات المتبعة والمتنوعة المستخدمة في عملية التصنيع على خواص الكاشف المصنَع, كذلك تأثير ابعاد ومحددات الكاشف على الاستجابة الطيفية له والمتمثلة بكفائة الكم.

في هذه الدراسة كان التركيز على كيفية التحكم في خواص الاستجابة الطيفية للكاشف الضوئي وذلك من خلال التحكم في بنية الكاشف نفسه, بتغيير نوع وتركيز الشوائب , كذلك بالتحكم في ابعاد الكاشف وغيرها من المواصفات. بالنسبة للكاشف المنفذ عمليا كان له منحنى استجابة طيفية يحتوي على استجابة عظمى واحدة وهي عند طول موجي 940nm تقريبا ومدى طيفي يمتد من 800nm الى 1100nm وهي نتائج مطابقة تقريبا للنتائج المحصلة من برنامج المحاكاة.

CONTENTS

SUBJECT **PAGE**

LIST OF FIGURES

LIST OF SYMBOLS

SYMBOL	DESCRIPTION
c_n	Electron capture coefficient
c_p	Hole capture coefficient
C_{dep}	Depletion layer capacitance
C_j	Junction capacitance
c	speed of light in vacuum
D_n	Diffusion coefficient of electrons
D_p	Diffusion coefficient of holes
E	electric field strength
E_g	Energy gap
E_t	Impurity level energy
E_c	Edge of conduction band
E_v	Edge of valence band
E_m	Maximum electric field in depletion-region
f_t	Occupation of impurity level
f_c	Cutoff frequency
$g_{n,max}$	Optical emission rates of electrons

$g_{p,max}$	Optical emission rates of holes
g_t	Impurity level degeneracy factor
G_e	Electron-hole generation rate
G	conductance
h	Planck constant
I_{sn}	Shot noise rms current
I_{jn}	Johnson noise rms current
I_{tn}	Total noise rms current
I_{sc}	Short circuit current
I_s	Reverse saturation current
J	current density
J_p	Hole current density
	Electron current densityJ_n
k	Boltzmann constant
L_p	Diffusion length of holes
N_t	Impurity concentration
n_n	Majority electron concentration
N_D	Donor impurities concentration

N_A	Accepter impurities concentration
N_c	Effective density of states in the CB
N_v	Effective density of states in the VB
n_f	Diode ideality factor
n_m	Refractive index
n_i	Intrinsic carrier concentration
n	Electron concentration
p_n	Minority hole concentration
p_{no}	Minority hole concentration at equilibrium
p	Hole concentration
p_{opt}	Optical power
Q	electric charge
q	Electron charge
G_{th}	Thermal generation rate
R_L	Load resistance
R_{ext}	External reflection at the surface of incidence
R_t	Internal reflection at the front surface
R_b	Internal reflection at the rear surface
R_e	Recombination rate

R_{ec}	Recombination coefficient
R_n	Recombination rate of electrons
R_p	Recombination rate of holes
R_{sh}	Shunt resistance
R_s	Series resistance
R	Reflection coefficient
S_{R0}	Photodetector responsivity at very low frequencies
S_n	Surface recombination velocity of minority carriers' electrons
S_p	Surface recombination velocity of minority carriers' holes
S_R	Photodetector Responsivity
T	Temperature
t	period of time
T_r	Rice time
Th_n	n- Layer thickness
Th_p	p- Layer thickness
U	The net recombination rate
v_{thn}	Electron thermal velocity

v_{thp}	Hole thermal velocity
ν	Light wave frequency
v_{bi}	Built-in potential barrier
V_R	Reverse biasing voltage
V_{bias}	reverse biasing voltage
V_D	Voltage across the p-n junction
V_{oc}	Open circuit voltage
W_D	Depletion layer width
x	distance
χ	Electron affinity
x_n	Space-charge width in the n-region
x_p	Space-charge width in the p-region
Δn	Excess electron concentration
Δp	Excess hole concentration
τ_p	Carrier lifetime for holes
τ_n	Carrier lifetime for electrons
τ_{n0}	SRH low-injection electron lifetime
τ_{p0}	SRH low-injection hole lifetime

α	Absorption coefficient
$\emptyset$	Photon flux
η	Quantum efficiency
σ_n^{opt}	Electron photoemission cross section of the impurity
σ_p^{opt}	Hole photoemission cross section of the impurity
λ	Free-space wavelength
α_n	Absorption coefficient for electron photoemission for the IPV impurity
α_p	Absorption coefficient for hole photoemission for the IPV impurity
α_{fc}	Absorption coefficient for free-carrier obsorption
α_{e-h}	Absorption coefficient for intrinsic band-to-band electron hole pair creation
α_{tot}	Total absorption coefficient
η_{max}	Maximum quantum efficiency
τ_{tr}	Transit time
τ_{RC}	Time constant of the equivalent circuit
Δf	Frequency bandwidth of photodetector
Ψ	electrostatic potential

μ_n	Electron mobility
μ_p	Hole mobility
ε_0	Permittivity in vacuum
ε_r	Relative permittivity
ε_s	Semiconductor Dielectric constant
ω	Angular frequency

LIST OF ABBREVIATIONS

ABBREVIATION	DESCRIPTION
A	Area
AC	Alternating Current
Al	Aluminum
AlGaAs	Aluminum Gallium Arsenide
AlGaN	Aluminum Gallium Nitride
AM	Air Mass
ASCII	American Standard Code for Information Interchange
a-Si:H	Hydrogenated amorphous Silicon
C-F	Capacitance-Frequency
CMOS	Complementary-Metal-Oxide-Semiconductor
CNT	Carbon Nano Tube
C-V	Capacitance-Voltage
CVI	C-language Virtual Instrumentation
DC	Direct Current
f	Frequency
FPA	Focal Plane Array

Ge	Germanium
HF	Hydrofluoric Acid
HgCdTe	Mercury Cadmium Telluride
In	Indium
InAs	Indium Arsenide
InSb	Indium Antimonide
IPV	Impurity Photovoltaic
IR	Infrared
IRFPA	Infrared Red Focal Plane Array
IrSi	Iridium Silicide
I-V	Current-Voltage
LED	Light-Emitting Diode
LWIR	Long Wavelength Infrared
MOCVD	Metal Organic Chemical Vapor Deposition
MSM	Metal-Semiconductor-Metal
MWIR	Medium Wavelength Infrared
NEP	Noise-Equation-Power
P	Vacuum Pressure
PbEuSe	Lead Europium Selenium
PbS	Lead Sulfide

PbSe	Lead Selenide
PbSnSe	Lead Tin Selenium
PbTe	Lead Telluride
PC	Photo Conductive
Pd_2Si	Palladium Silicide
PtSi	Platinum Silicide
PV	Photovoltaic
QE	Quantum Efficiency
QW	Quantum Well
QWIP	Quantum Well IR Photodetectors
R	Rate of deposition
r.m.s	Root-Meat-Square
RCED	Resonant Cavity Enhanced Detector
SCAPS	Solar cell CAPacitance Simulator
Si	Silicon
SiO_2	Silicon Dioxide
SNR	Signal-to-Noise Ratio
SRH	Shockley-Read-Hall
TH	Thickness
Ts	Substrate temperature

VLWIR	Very Long Wavelength Infrared
WKB	Wentzel–Kramers–Brillouin

ABSTRACT

In this work a study and implementation of indium-doped silicon infrared photodetector has been done. The incorporation of indium into silicon will affect the detector spectral response due to its role as a generation-recombination center.

A computer simulation program called SCAPS has been used to investigate the indium doped silicon infrared detector, which is one of the modern programs used to simulate and analyze the semiconductor devices operations.

By using Balzers coating system BA510 vacuum evaporation technique, the fabrication of indium doped silicon photodiode has been performed and the effect of fabrication process procedures on the characteristics of the photodetector has been investigated. The effect of geometries and parameters of the indium doped silicon photodiode on the photodetector's spectral response, which is represented here as the quantum efficiency, is studied and investigated.

This study focuses on the spectral response of the photodetector and how to adjust it through adjusting the structure of the photodetector itself, by controlling the trap type and density, also by controlling the detector's dimensions and other. For the practically worked photodetector, the spectral response curve has one peak at approximately 940nm and a spectral range from about 800nm to 1100nm. This approximately identical to the simulated photodetector.

The results obtained are discussed and conclusions have been given, suggestions are given for future work in this field.

CHAPTER ONE

INTRODUCTION AND LITERATURE REVIEW

1.1 INTRODUCTION

Photodetector is an optical receiver which transforms the energy of optical radiation (such as infrared, visible light or ultraviolet) into the electrical signal that is convenient for measurements. Infrared radiation is the electromagnetic waves in the wavelength region longer than the visible light wavelengths, lying from 0.75 μm (1.65eV) to 1000 μm (1.2meV). The wavelength region of 0.75 μm to 3μm is often called the near infrared, the wavelength region of 3 μm to 6μm is the middle infrared, and the wavelength region of 6 μm to 15 μm is the far infrared. Also, even longer wavelength regions are sometimes referred to as ultra far infrared, but this is not a universally accepted term. Infrared radiation has the following characteristics [1]:

1. Invisible to human eyes: This is useful for security applications.
2. Small energy: Infrared radiation energy is equal to the vibrational or rotational energy of molecules. This phenomenon makes it possible to identify molecules.
3. Long wavelength: This means that infrared radiation is less scattered and offers better transmission through various medium.
4. Emitted from all kinds of objects: All objects with an absolute temperature of over 0 K radiate infrared energy.

Infrared radiation is extensively used in many applications, where, in the spectral range of (0.78-3.0μm) IR detectors are used for applications as diverse as fiber optic communications, agricultural sorting, environmental monitoring, and chemical analysis. Further into the IR region (from 2-5μm), applications for IR detectors include non-contact temperature sensing, thermal imaging, and gas analysis for pollution control [2]. The large variety of photodetectors is required

because photodetectors target different aspects of applications. To choose a photodetector for a specific application, the first criteria are the applicable range of wavelengths, the response speed and the cost.

The performance of the photodetector depends on the flux and distribution of light intensity within the structure under examination as well as on the material and electronic parameters, such as band structures and doping levels. Depending on the application, the performance refers to sensitivity, short response times, wavelength selectivity and other characteristics. To optimize the performance of the detector element, one can influence the light intensity distribution within, which, in turn, depends on the geometric and optical parameters of the structure as well as on the properties of the incident radiation.

Computer simulations can significantly speed-up the design process. If such simulations are to provide useful information, however, the simulations need to take into account all important of the factors that influence the device performance [3].

1.2 LITERATURE REVIEW

The birth of the photodetector can be dated back to 1873 when W. Smith discovered photoconductivity in selenium. The progress of photodetectors was slow until Einstein explained the newly observed photoelectric effect in metals, and Planck solved the black body emission puzzle by introducing the quanta hypothesis [3].

Modern history of IR detectors commenced with the development of first IR detector by Case in 1917. He discovered that a

substance made of thallium and sulphur exhibited photoconductivity. Later, he found that addition of oxygen enhanced the response.

World War II stirred further research in detectors. In 1940s Photon detectors were developed to improve sensitivity and response time. Lead sulfide (PbS) was the first practical IR detector. PbS is sensitive to infrared wavelengths up to 3μm. This detector was deployed in a variety of applications in the World War II.

Beginning in the late 1940s and continuing into 1950s, a wide variety of new materials was developed for IR sensing. Lead Selenide (PbSe) and lead telluride (PbTe) extended the spectral range beyond that of PbS, providing sensitivity in the 3-5μm Medium Wavelength Infrared (MWIR) atmospheric window. The extrinsic photoconductive (PC) response from copper, zinc and gold impurity levels in germanium made devices possible in the 8-14μm Long Wavelength (LWIR) spectral window and beyond to Very Long Wavelength (VLWIR) region. The end of the 1950s saw the first introduction of semiconductor alloys, in the chemical table group III-V, IV-VI, and II-VI material systems. One such material was indium antimonide (InSb). It had advantages of small energy gap and it could be prepared in a single crystal form. These alloys allowed the bandgap of the semiconductor, and hence its spectral response, to be custom tailored for specific applications [2].

In 1969 the properties of the alloy semiconductor $Hg_{1-x}Cd_xTe$ and its application as an infrared photoconductive detector material were reviewed by Ernie L. Stelzer et al. [4]. They had first established the motivating reasons for selecting intrinsic $Hg_{1-x}Cd_xTe$ for an infrared detector material, Where $Hg_{1-x}Cd_xTe$ is a variable gap

semiconductor, direct energy gap, ability to obtain both low and high carrier concentrations, high mobility of electrons and low dielectric constant [5]. These potential advantages were verified by experimental results that indicated a detectivity approaching the theoretical limit. Therefore this alloy system presents the possibility of fabricating detectors having different peak responses.

In 1990 Tsaur, Chen and Nechay [6] have been fabricated a Schottky barrier infrared detector with a 4 nm thick IrSi electrode on p-type Si substrate previously implanted with low energy boron ions. The shallow boron-doped P^+ layer increases the image-force barrier lowering and field-assisted tunneling, thereby reducing the electrical barrier height to only 0.094ev. The optical barrier height, found by spectral response measurements, is 0.1ev, which corresponds to a detector cutoff wavelength of 12.4 μm. To first order, the barrier height of an intimate silicide/Si Schottky contact is determined by the intrinsic properties of the silicide and Si, however the height also depends on the substrate doping profile. FPAs incorporating such detectors are potentially useful for thermal imaging of objects at or below room temperature in a low-background environment.

By employing a thin silicon sacrificial cap layer for silicide formation, Xiao et al. [7] in 1993 had successfully demonstrating $Pd_2Si/Strained\ Si_{1-x}Ge_x$ Schottky barrier infrared detector with extended cutoff wavelengths. The sacrificial silicon eliminates the segregation effects and Fermi-level pinning which occur if the metal reacts directly with the $Si_{1-x}Ge_x$ alloy. The Schottky barrier height of the $Silicide/Strained\ Si_{1-x}Ge_x$ detector decreases with increases Ge fraction, allowing for tuning of the detector cutoff wavelength. The

cutoff wavelength has been extended beyond 8μm in $PtSi/Si_{0.85}Ge_{0.15}$ detectors. They have shown that high quantum efficiency and near-ideal dark current can be obtained from these detectors.

In 1994 Waldemar Gawron, Jozef Piotrowski [8] have been reported near room temperature LWIR photodiodes, which operation has been extended to room temperature. This was achieved by a special design of active elements and by the use of optical immersion. Large area devices can be produced by using close-spaced elements connected in series to increase the voltage responsivity. Practical $Hg_{1-x}Cd_xTe$ devices have been obtained and characterized. The performances of the devices have been improved by the use of optical immersion and other means. The devices can be used for various applications, where high speed of response from one side and absence of low frequency noise from the other is essential.

In 2005 S. V. Bandara et al. [9] studied the spectral response of Quantum Well Infrared Photodetectors (QWIPs) based on the III-V material system which is tailorable to narrow or broad bandwidths within mid- and long-wavelength infrared bands. Typical broadband QWIPs show considerable spectral shape change with bias voltage, particularly near the cutoff wavelength region. Two alternatives to the typical broadband QWIP design have been demonstrated. These designs consist of two multi quantum well (QW) stacks or alternatively placed QWs and produce nearly fixed spectrums within the operating bias voltages. Flexibility in many design parameters of these detectors allows for tuning and tailoring the spectral shape

according to application requirements, specifically for spectral imaging instruments.

In 2005 N. Biyikli et al. [10], fabricated and tested Solar-blind metal- semiconductor-metal (MSM) photodiodes based on Metal Organic Chemical Vapor Deposition MOCVD-grown $Al_{0.6}Ga_{0.4}N$ template. AlGaN detector samples were fabricated by using a microwave compatible fabrication process. Optical transmission, current-voltage, spectral responsivity, and temporal pulse response measurements were carried out. The fabricated devices had very low leakage current and displayed true solar-blind response with ~255 nm cutoff wavelength.

Narrow spectral band infrared detectors are required for multispectral infrared imaging, wavelength selectivity can be obtained by placing passive line filters in front of the detectors, or, the preferred choice, by making the detectors themselves wavelength selective, in 2006 a paper published by H. Zogg and M. Arnold [11], a Resonant Cavity Enhanced Detectors (RCED) with high quantum efficiencies and one single narrow spectral line had been realized for the first time in the mid-IR range. The detectors consist of narrow gap lead chalcogenides grown on Silicon substrates. The peak wavelength is determined by the design of the cavity and may be chosen anywhere between 3 μm and > 15 μm by using appropriate compositions $Pb_{1-x}Y_xSe$ (Y = Eu, Sn) of the absorber layer. Applications are for IR hyperspectral imaging as well as for spectroscopy.

In 2006 a study on silicon p-n junction photodetectors had been done by Xian Song Fu et al. [12] wherein on the basis of n-type single

crystal (100) silicon substrate; a silicon p-n junction photodetector has been successfully developed. Three methods to improve photoresponse Signal-to-Noise Ratio (SNR) were profoundly studied: the p-n junction depth was optimized to enhance the spectral responsivity within the wavelength range of 500-600 nm, an antireflection layer with the appropriate thickness was added to reduce the reflected light and enhance the sensitivity, the adjustment technique of spectral band response was adopted to remove the noise signal with normal silicon absorptive wavelengths. Eventually, the spectral responsivity SNR can be over 10^4 at 500-600 nm while the peak of spectral responsivity is 0.48 A/W at about 520 nm. After being optimized, silicon p-n junction photodetectors, which possess the properties of lower dark current, higher sensitivity, shorter response time and larger SNR, can be achieved.

In 2007 P. Louro et al. [13], reported an amorphous silicon (Hydrogenated amorphous silicon (a-Si: H)) based image sensor with a bias voltage controllable spectral response characteristics. This multilayered device is composed by two stacked p-i-n-i-p structures produced by plasma enhanced chemical vapor deposition on a glass substrate and sandwiched between two transparent conductive oxide electrodes with a patterned molybdenum layer between the sensing and switching structures (To reduce the optical coupling between the sensing and the switching diodes). Optical readout technique is used for image readout. Device performances have been evaluated from the current -voltage characteristics and spectral response measurements performed for the p-i-n-i-p test structures and stacked device. It is demonstrated that the device is sensitive to blue–green or red light depending on polarity of the bias voltage enabling the detection of

color images. Device design is discussed and supported by a numerical simulation.

As a promising nano material, Carbon Nano Tube (CNT) has been studied for infrared sensing with its unique properties such as wide range of band gaps and reduced carrier scattering, however, due to the traditional inefficient and unreliable fabrication process, the research of CNT based infrared sensors remained on the single pixel study, which significantly limited the further investigation and application of CNTs in infrared sensing, in the study by Jiangbo Zhang et al. in 2008 [14], an efficient and controllable nano manufacturing process was developed, and a CNT based three-pixel IR detector array with a 10 μm pixel pitch was fabricated by using this nano manufacturing process. The experimental testing on the electronic and photonic properties of each pixel shows that CNT formed a Schottky junction with the contact metal. And the photovoltaic effect of each Schottky junction was used to detect IR. It has also been shown that the CNT detector array is able to detect special variance of incident IR power density and has small thermal cross talk between adjacent pixels, which makes CNT a promising material for high resolution Infrared Focal Plane array IRFPAs.

In 2010, O. Thomas et al. [15], demonstrated an efficient photon number detector for visible wavelengths by using a silicon avalanche photodiode. Si-APDs under short excess bias pulses can be used for photon number detection with high detection efficiency in a practical, thermoelectrically cooled device. The detector is attractive for quantum information applications requiring single-shot photon number detection at high repetition rates (For some advanced functions, these detectors must be able to resolve the number of

photons in an optical pulse). By measuring the photosensitivity of the APD at dc biases far below the breakdown voltage, for which the gain is unity, the external QE of the complete system was determined to be 81±1% at a wavelength of 600 nm. This represents the highest obtainable single photon detection efficiency with this device at this wavelength. The quantum efficiency can be improved, to a value close to unity, by optimizing the optical coupling, reducing reflection at the front surface and increasing the thickness of the absorbing layer in the APD. The surface microstructure can also be engineered to enhance the absorption.

In 2010 Yasuhiko Ishikawa, Kazumi Wada [16], published a paper describes that Ge plays an enabler to integrate active photonic devices on a Si platform (Si photonics is a technology to integrate photonics on a Si complementary metal-oxide-semiconductor (CMOS) platform). In spite of the large lattice mismatch of ~4% between Ge and Si, high-quality Ge layers can be epitaxially grown on Si by ultrahigh-vacuum chemical vapor deposition. Applications of the Ge layers to near-infrared active photonic devices, i.e., photodiodes, optical modulators and light emitters, are described. Several issues on the device physics as well as the integration with Si electronics are discussed.

In 2010 Christina F. de Souza et al. [17], report on measurements of the infrared photo-response of InAs-based p-i-n diodes in the spectral region above 1.8 μm. These photodiodes were fabricated from arrays of InAs quantum dots (InAs quantum dots embedded in an AlGaAs-based heterostructure) grown in nano-patterned template structures by using a combination of block copolymer lithography and molecular beam epitaxy. The devices

studied, were comprised of a single layer of quantum dots. The temperature dependence of the current versus voltage for these devices is presented and discussed. Finally, a model is presented that can explain the key characteristics of the measured current versus voltage curves as a function of both temperature and applied electric field.

1.3 THE AIM OF THE PRESENT WORK

The overall aim of this thesis is to study the silicon p-n junction with indium as the p-type doping, to implement near infrared detector, adjusting the wavelength selectivity and spectral responsivity range of this detector practically and via the simulation.

1.4 THESIS SCOPE

Chapter two includes most of the theoretical information needed to understand and characterize infrared photodetectors in general.

Chapter three describes the tools which have been used to implement and characterize the infrared photodetectors, including the simulation program SCAPS.

Chapter four contains the simulation results about the spectral response of the infrared photodetectors and their discussion.

Chapter five contains the practical results obtained and their discussions, including I-V and spectral response measurements.

And finally, chapter six discusses the conclusions and suggestions for future works.

CHAPTER TWO

ESSENTIALS AND THEORETICAL BACKGROUND OF PHOTODETECTORS

2.1 INTRODUCTION

Photodetectors are semiconductor devices that can detect optical signals through electronic processes. The operation of a general photodetector includes basically three processes:

1- Carrier generation by incident light.

2- Carrier transport.

3- Extraction of carriers as terminal current to provide the output signal.

Photodetectors are important in optical-fiber communication systems operated in the near-infrared region (0.8-1.6μm). They demodulate optical signals, that is, convert the optical variations into electrical variations that are subsequently amplified and further processed. For such applications, the photodetectors must satisfy stringent requirements such as high sensitivity at operating wavelengths, high response speed, and minimum noise. In addition, the photodetector should be compact in size, uses low biasing voltage and current, and should be reliable under operating conditions [18].

2.2 PHOTODIODE OPERATION

Figure (2.1) shows a cross section of a photodiode. The p-layer material at the active surface and the n-layer material at the substrate form a p-n junction which operates as a photoelectric converter. By controlling the thickness of the outer layer (p-layer), substrate (n-layer) and as well as the doping concentration, the spectral response and frequency response can be controlled. When light strikes a photodiode, the electron within the crystal structure becomes stimulated. If the light energy is greater than the band gap energy (E_g),

the electrons are pulled up into the conduction band, leaving holes in their place in the valence band as shown in figure (2.2).

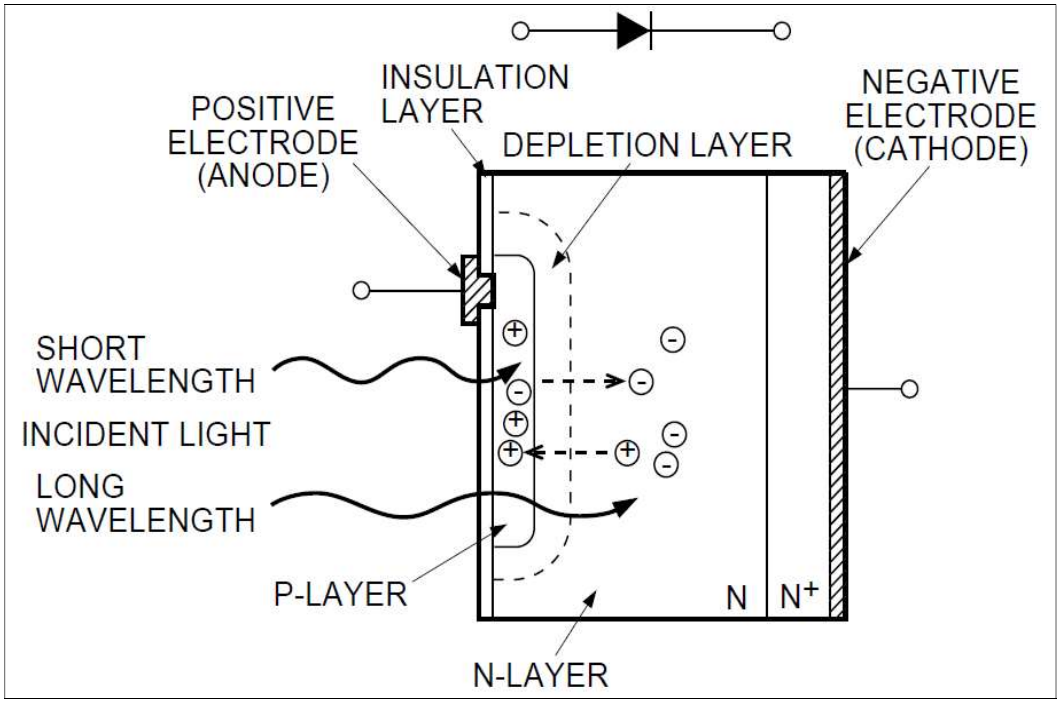

Figure (2.1) a cross section of a photodiode

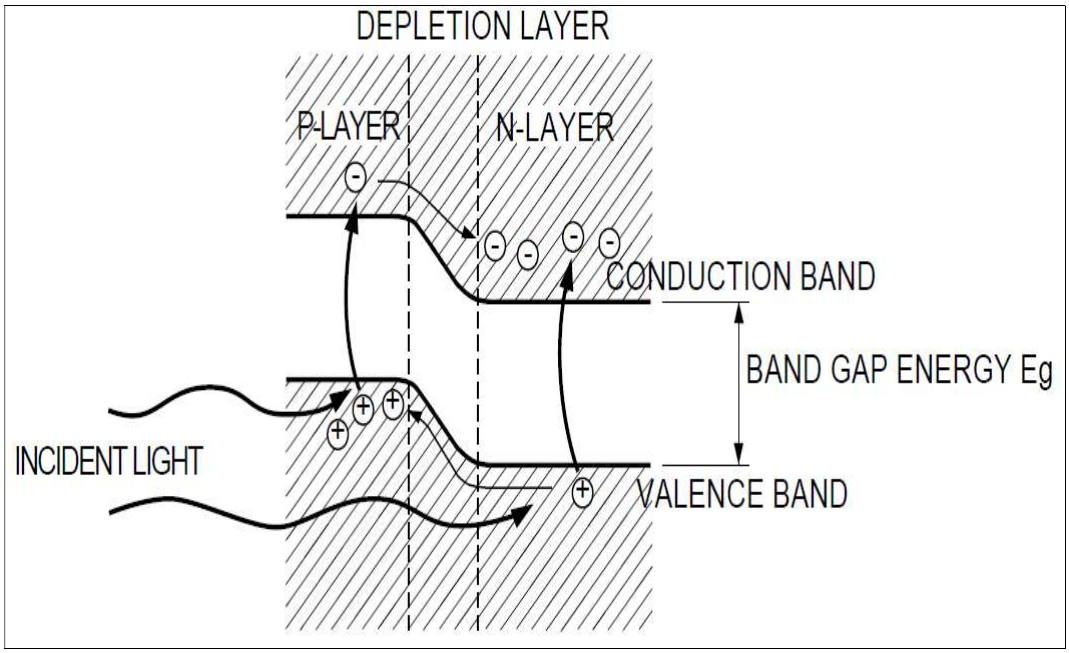

Figure (2.2) energy bands diagram in the photodiode with zero biasing

These electron-hole pair creations occur throughout the p-layer, depletion layer and n-layer materials. In the depletion layer the electric field accelerates these electrons toward the n-layer and the holes toward the p-layer. Of the electron-hole pairs generated in the n-layer, the electrons, along with electrons that have arrived from the p-layer, are left in the n-layer conduction band. The holes at this time are being diffused through the n-layer up to the depletion layer while being accelerated, and collected in the p-layer valence band. In this manner, electron-hole pairs which are generated in proportion to the amount of incident light are collected in the n- and p-layers. This results in a positive charge in the p-layer and a negative charge in the n-layer. If an external circuit is connected between the p- and n-layers, electrons will flow away from the n-layer, and holes will flow away from the p-layer toward the opposite respective electrodes. These electrons and holes generating a current flow in a semiconductor are called the carriers [19].

2.3 INTERACTION BETWEEN LIGHT AND SEMICONDUCTOR

When photons of light strike the detector surface, some of the light is reflected from the front surface, while the rest enters the medium and propagates through it. If any of this light reaches the back surface, it can be reflected again, or it can be transmitted through to the other side. The amount of light transmitted is therefore related to the reflectivity at the front and back surfaces and also to the way the light propagates through the medium [20].

2.3.1 THE ABSORPTION OF LIGHT IN A SEMICONDUCTOR

Absorption occurs during the propagation of light through the medium if the frequency of the light is resonant with the transition frequencies of the atoms in the medium [20]. In this case, the light will be attenuated as it progresses. The transmission of the medium is clearly related to the absorption, because only unabsorbed light will be transmitted. Selective absorption is responsible for the coloration of many optical materials, rubies for example are red because they absorb blue and green light but not red. The absorption of light by an optical medium is quantified by its absorption coefficient (α); this is defined as the fraction of the power absorbed in a unit length of the medium. The absorption of a flux of photon ϕ passing through a differential thickness element dl is expressed by [20]:

$$d\phi = -\alpha(\lambda)\, \phi\, dl \qquad \ldots(2.1)$$

With the solution for the remaining flux at depth l being

$$\phi = \phi_o\, e^{-\alpha(\lambda) l} \qquad \ldots(2.2)$$

Where ϕ_o is the flux entering the detector. The absorption coefficient is a strong function of light wavelength, so that optical materials may absorb one color but not another.

Absorption coefficient not only determines whether light can be absorbed for photoexcitation, but it also indicates where light is absorbed. A high value of absorption coefficient indicates that light is absorbed near the surface where light enters. A low value means that the absorption is low so that, light can penetrate deeper into the semiconductor. In the extreme, light can be transparent for long wavelengths without photoexcitation. Thus the absorption coefficient determines the quantum efficiency of a photodetector [18], where the

quantum efficiency (η) is given by the flux absorbed in the detector divided by the total flux incident on its surface, that is [21]:

$$\eta = \frac{\phi_o - \phi_o e^{-\alpha(\lambda)d}}{\phi_o} = 1 - e^{-\alpha(\lambda)d} \quad \ldots(2.3)$$

Where d is the thickness of the detector ($l = d$).

The total absorption coefficient in the detector's cell α_{tot} includes all the absorption processes which are [22]:

$$\alpha_{tot}(\lambda) = \alpha_n(\lambda) + \alpha_p(\lambda) + \alpha_{fc}(\lambda) + \alpha_{e-h}(\lambda) \quad \ldots(2.4)$$

$$\alpha_n(\lambda) = f_t N_t \sigma_n^{opt}(\lambda) \quad \ldots(2.5)$$

$$\alpha_p(\lambda) = (1 - f_t) N_t \sigma_p^{opt}(\lambda) \quad \ldots(2.6)$$

$$\alpha_{fc}(\lambda) = (2.7 \times 10^{-18} p + 1.8 \times 10^{-18} n)\lambda^2 \quad \ldots(2.7)$$

Where:

α_n: is the absorption coefficient for electron photoemission from the IPV impurity (process 2 of figure 2.3).

α_p: represents the hole photoemission from the IPV impurity (process 1 of figure 2.3).

α_{fc}: is the absorption coefficient for free-carrier absorption, a process which doesn't result in the creation of electron-hole pairs.

α_{e-h}: is the absorption coefficient for intrinsic band-to-band electron-hole pair creation (process 3 of figure 2.3).

f_t **:** is the occupancy of the impurity level.

N_t : is the impurity concentration.

σ_n^{opt} : is the electron photoemission cross section of the impurity.

σ_p^{opt} : is the hole photoemission cross section of the impurity.

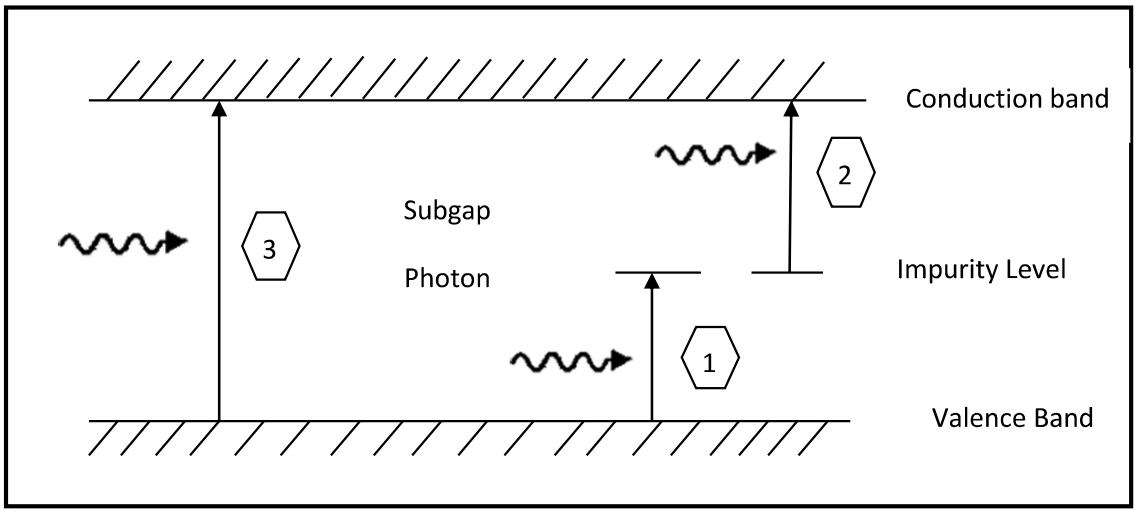

Figure (2.3) the impurity photovoltaic effect: subgap photons create electron-hole pairs via impurity level (1) and (2). Compared to intrinsic band to band absorption (3)

n : is the electron concentration.

p : is the hole concentration.

λ : is the free-space wavelength.

2.3.2 REFLECTION

Photons are lost by reflection from the surface before they enter the detector volume, leading to a reduction in quantum efficiency (η). Minimal reflection occurs for photons striking at normal incidence [21].

$$R = \frac{(n_m - 1)^2 + (\alpha(\lambda)\lambda/4\pi)^2}{(n_m + 1)^2 + (\alpha(\lambda)\lambda/4\pi)^2} \quad \ldots(2.8)$$

Where:

R, is the reflectivity, which is the fraction of the incident flux of photons that is reflected; n_m, is the refractive index of the material, (which is speed of light in vacuum/speed of light in the material), α (λ), is the absorption coefficient at wavelength λ, and it is assumed that the photon is incident from air or vacuum, which has a refractive index of $n_m \approx 1$.

In the detector cell there are three reflection processes:

1- External reflection at the surface of incidence (R_{ext}).

2- Internal reflection at the front surface (R_t).

3- Internal reflection at the rear surface (R_b).

The degree of light trapping is adjusted by the parameter (R_b), where light trapping effectively enhances the photon flux inside the cell.

2.4 GENERATION AND RECOMBINATION IN SEMICONDUCTORS

Whenever the thermal equilibrium condition of a semiconductor system is disturbed (which means $pn \neq n_i^2$), processes exist to restore the system to equilibrium (which means $pn = n_i^2$). These processes are recombination when $(pn > n_i^2)$ and thermal generation when $(pn < n_i^2)$. The energy of an electron in transition from the conduction band to the valence band is conserved by emission of a photon (radiative process) or by transfer of the energy to another free electron or hole (Auger process). The former process is the inverse of direct optical absorption, and the latter is the inverse of impact ionization [18].

2.4.1 BAND-TO-BAND OR INTRINSIC GENERATION / RECOMBINATION PROCESS

Band-to-band transitions are more probable for direct-bandgap semiconductors. For this type of transition, shown in figure (2.4), the recombination rate is proportional to the product of electron and hole concentrations, given by

$$R_e = R_{ec} pn \quad \ldots(2.9)$$

The term R_{ec}, called the recombination coefficient, is related to the thermal generation rate G_{th}, by

$$R_{ec} = G_{th}/n_i^2 \quad \ldots(2.10)$$

R_{ec} is a function of temperature and is also dependent on the band structure of the semiconductor. A direct bandgap semiconductor, being more efficient in band-to-band transitions, has a much larger R_{ec} $(\approx 10^{-10}\, cm^3/s)$ than an indirect-bandgap semiconductor $(\approx 10^{-15}\, cm^3/s)$. In thermal equilibrium, since $pn = n_i^2$, then $R_e = G_{th}$ and the net recombination rate $U(= R_e - G_{th})$ equals zero. Under low-level injection, defined as the case where the excess carriers $\Delta p = \Delta n$ are fewer than the majority carriers, for an n-type material, $p_n = p_{n0} + \Delta p$ and $n_n \approx N_D$, the net recombination rate is given by [18]:

$$U = R_e - G_{th} = R_{ec}\left(pn - n_i^2\right) \quad \ldots(2.11)$$

$$U \approx R_{ec} \Delta p N_D \equiv \frac{\Delta p}{\tau_p} \quad \ldots(2.12)$$

Where the carrier lifetime for holes (τ_p) is given by:

$$\tau_p = \frac{1}{R_{ec} N_D} \quad \ldots(2.13)$$

And in p-type material, the carrier lifetime for electrons (τ_n) is given by:

$$\tau_n = \frac{1}{R_{ec} N_A} \qquad \ldots (2.14)$$

Where N_D, is the n-type donor impurities concentration, N_A is the p-type acceptor impurities concentration, and n_i is the intrinsic or equilibrium carriers concentration.

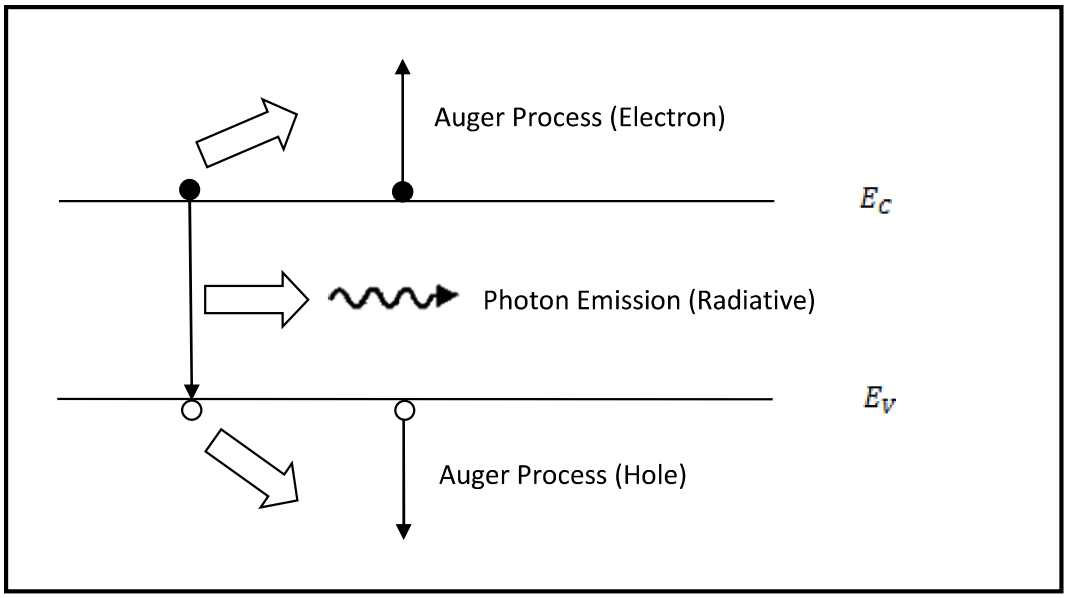

Figure (2.4) band-to-band recombination processes (energy is exchanged to a radiative or Auger process)

2.4.2 MODIFIED SHOCKLEY-READ-HALL OR EXTRINSIC GENERATION / RECOMBINATION PROCESSES

The six impurity-related transitions included in the modified SRH model are shown in figure (2.5). For steady state conditions, the net recombination rate (U) via an impurity level is given by [22]:

$$U = \frac{np - n_1^* p_1^*}{\tau_{n0}(p + p_1^*) + \tau_{p0}(n + n_1^*)} \qquad \ldots (2.15)$$

Where:

$$\tau_{n0} = 1/c_n N_t \quad \ldots(2.16)$$

$$\tau_{p0} = 1/c_p N_t \quad \ldots(2.17)$$

$$n_1^* = n_1 + \tau_{n0}\, g_{n,max} \quad \ldots(2.18)$$

$$p_1^* = p_1 + \tau_{p0}\, g_{p,max} \quad \ldots(2.19)$$

$$n_1 = g_t\, N_c\, e^{-(E_c - E_t)/kT} \quad \ldots(2.20)$$

$$p_1 = \frac{1}{g_t}\, N_v\, e^{-(E_t - E_v)/kT} \quad \ldots(2.21)$$

$$g_{n,max} = N_t \int_{\lambda_g}^{\lambda_{n,max}} 2\sigma_n^{opt}(\lambda)\, \phi_{ph}(x,\lambda)\, d\lambda \quad \ldots(2.22)$$

$$g_{p,max} = N_t \int_{\lambda_g}^{\lambda_{p,max}} 2\sigma_p^{opt}(\lambda)\, \phi_{ph}(x,\lambda)\, d\lambda \quad \ldots(2.23)$$

With the occupancy of the impurity level (f_t) given by [22]:

$$f_t = \frac{c_n n N_t + c_p p_1 N_t + g_{p,max}}{c_n N_t (n + n_1) + \left(g_{n,max} + g_{p,max}\right) + c_p N_t (p + p_1)} \quad \ldots(2.24)$$

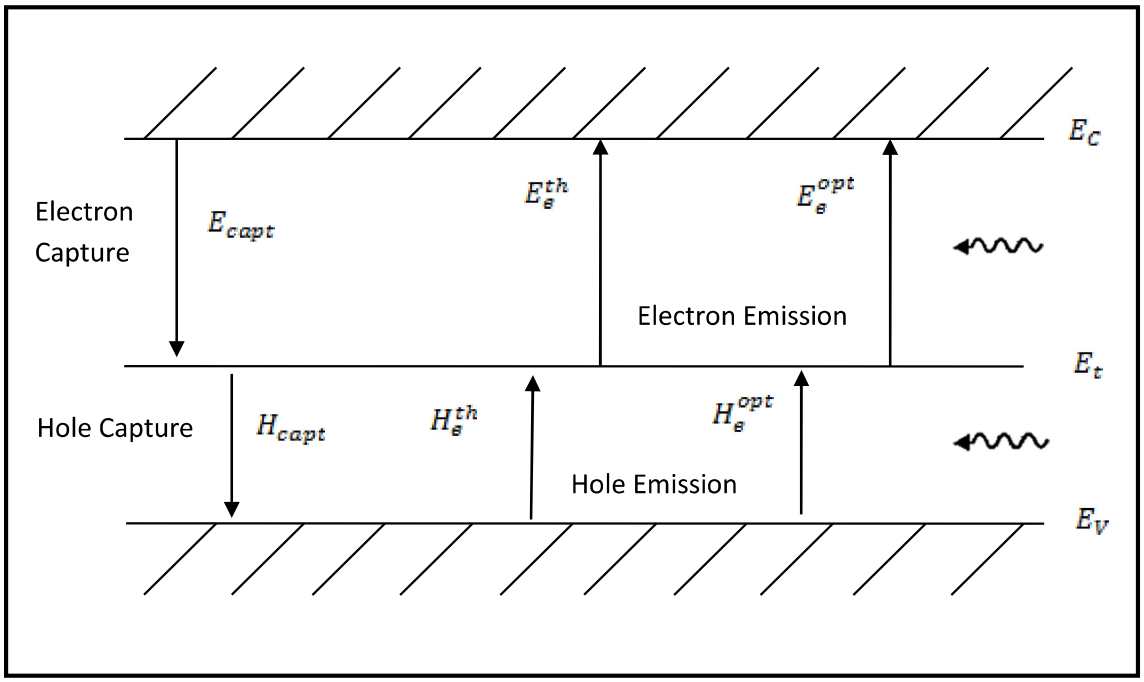

Figure (2.5) : The six transitions of the modified SRH recombination model. Electron and hole emission can occur thermally (th) or optically (opt).

Equation (2.15) is widely applicable, nondegeneracy being the major assumption. n and p are the electron and hole concentrations, τ_{n0} and τ_{p0} are the SRH low-injection lifetimes for electrons and holes, $\mathrm{N_t}$ is the impurity concentration, $\mathrm{c_n}$ and $\mathrm{c_p}$ are the electron and hole capture coefficients, g_t is the impurity-level degeneracy factor and E_t the impurity-level energy, E_c and E_v are the conduction and valence band edges respectively, and N_c and N_v are the effective densities of states in the conduction and valence bands. $g_{n,max}$ is the optical emission rate of electrons from the impurity (process 2 of Figure 2.3), with the impurity fully occupied. $g_{p,max}$ is the optical emission rate of holes from the impurity (process 1 of Figure 2.3) , with the impurity completely empty. $\sigma_{\mathrm{n}}^{\mathrm{opt}}(\lambda)$ and $\sigma_{\mathrm{p}}^{\mathrm{opt}}(\lambda)$ are the electron and hole photoemission cross sections of the impurity, with thresholds at $\lambda_{n,max}$ and $\lambda_{p,max}$ respectively. The lower limit on the wavelength integrations is assumed to be the silicon bandgap wavelength $\lambda_{\mathrm{g}} = 1.107\ \mu\mathrm{m}$. It is assumed that all shorter-wavelength photons are utilized by intrinsic band-to-band absorption (process 3 of Figure 2.3). $\phi_{ph}(x,\lambda)$ is the photon flux density at a distance x from the illuminated front surface. The factor 2 is a geometrical factor to account for the oblique passage of light within the textured cell considered.

The lifetime arising from indirect transitions is inversely proportional to the trap density N_t while in the band-to-band transition case the lifetime from direct transitions is inversely proportional to the doping concentration. Many impurities have energy levels close to the middle of the bandgap; these impurities are efficient recombination centers. A typical example is gold in silicon, the minority-carrier lifetime decreases linearly with the gold concentration over the range of 10^{14} to $10^{17}cm^{-3}$, where τ decreases from about $2 \times 10^{-6}s$ to $2 \times 10^{-9}s$. This effect is sometimes advantageous, as in some high-speed applications when a short lifetime to reduce the charge storage time is a desirable feature [18].

2.5 THE IMPURITY PHOTOVOLTAIC (IPV) EFFECT

The impurity photovoltaic effect is defined as the deliberate incorporation of impurities into a device to allow carrier generation via impurity levels. The subgap photons create electron-hole pairs via impurity levels, enabling an otherwise wasted portion of the spectrum to contribute to cell output.

The recombination rate U may be negative indicating improved current generation, or may be positive, indicating increased recombination process. The consideration of the trade-off between optical and thermal emission processes for different impurity level positions in the bandgap is very necessary for deciding which impurity to investigate.

The midgap impurity will maximize the amount of the subgap spectrum, so that the upper limit on the wavelength integration (equations 2.22 and 2.23) $\lambda_{n,max}$ and $\lambda_{p,max}$ both correspond to half

the bandgap energy. Consequently the electron-hole pair creation will then relay on two weak optical processes, described as follows:

In order to make the recombination rate U negative, this requires

$$np - n_1^* p_1^* < 0 \qquad \ldots (2.25)$$

The magnitude of the product term $n_1^* p_1^*$ depends on the particular choice of impurity, and for U to be negative $n_1^* p_1^*$ must be as large as possible, equation (2.25) can be written as:

$$np - \left(n_1 + \tau_{n0} g_{n,max}\right)\left(p_1 + \tau_{p0} g_{p,max}\right) < 0 \qquad \ldots (2.26)$$

Thermal emission rates are proportional to n_1 and p_1, which depend strongly on the impurity level position in the bandgap. For midgap impurity levels $n_1 \cong p_1 \cong n_i$ and therefore place strong requirements on both the photoemission terms in equation above.

A shallow impurity level gives rise to an asymmetry between n_1 and p_1. For shallow acceptor $p_1 \gg n_1$, which means that only one of the photoexcitation processes is crucial for $n_1^* p_1^*$ to be large i.e. $g_{n,max}$. So the shallow impurity leaves only one of the two steps dependent on weak optical excitation. Indium is considered as a deep-level impurity which provides both reasonable access to the subgap spectrum, and depend on only one of the weak impurity optical processes. It is a medium-deep acceptor impurity in silicon, with a level energy 157 m eV above the valence-band edge as shown in figure (2.6) [23].

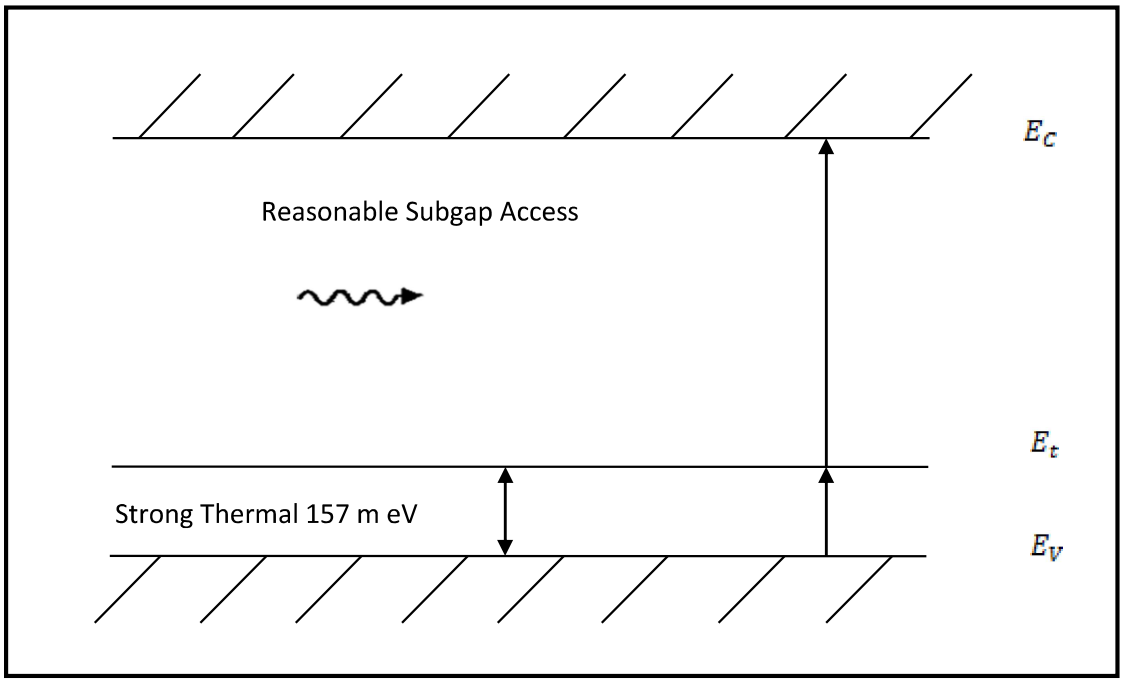

Figure (2.6) Indium as a mid-deep level impurity.

2.6 THE TOTAL PHOTOCURRENT DENSITY

Under steady state conditions the total photocurrent density through the depletion layer is given by:

$$J_{tot} = J_{drift} + J_{diffusion} \quad \ldots(2.27)$$

where J_{drift} is the drift current density due to carriers generated within the depletion region and $J_{diffusion}$ is the diffusion current density due to carriers generated outside the depletion region in the bulk of the semiconductor and diffusing into the junction. A derivation of the total current will be done under the assumptions that the thermal generation current can be neglected and that the surface p-layer is much thinner than $1/\alpha$. Referring to figure (2.7), the electron-hole generation rate is given by [18]:

$$G_e(x) = \phi_o \, \alpha \, exp(-\alpha x) \quad \ldots(2.28)$$

Where ϕ_o is the incident photon flux per unit area which is given by:

$$\phi_o = P_{opt}(1-R)/Ahv \quad \ldots(2.29)$$

R is the reflection coefficient, and A is the device area. The drift current J_{drift} is thus given by [18]:

$$J_{drift} = -q\int_0^{W_D} G_e(x)\,dx = q\phi_o[1-exp(-\alpha W_D)] \quad \ldots(2.30)$$

Where W_D is the depletion region width. Noted that within the depletion region, a quantum efficiency of 100% has been assumed.

For x > W_D, the minority-carrier density (holes) in the bulk semiconductor is determined by the one-dimensional diffusion equation:

$$D_p\frac{\partial^2 P_n}{\partial x^2} - \frac{P_n - P_{n0}}{\tau_p} + G_e(x) = 0 \quad \ldots(2.31)$$

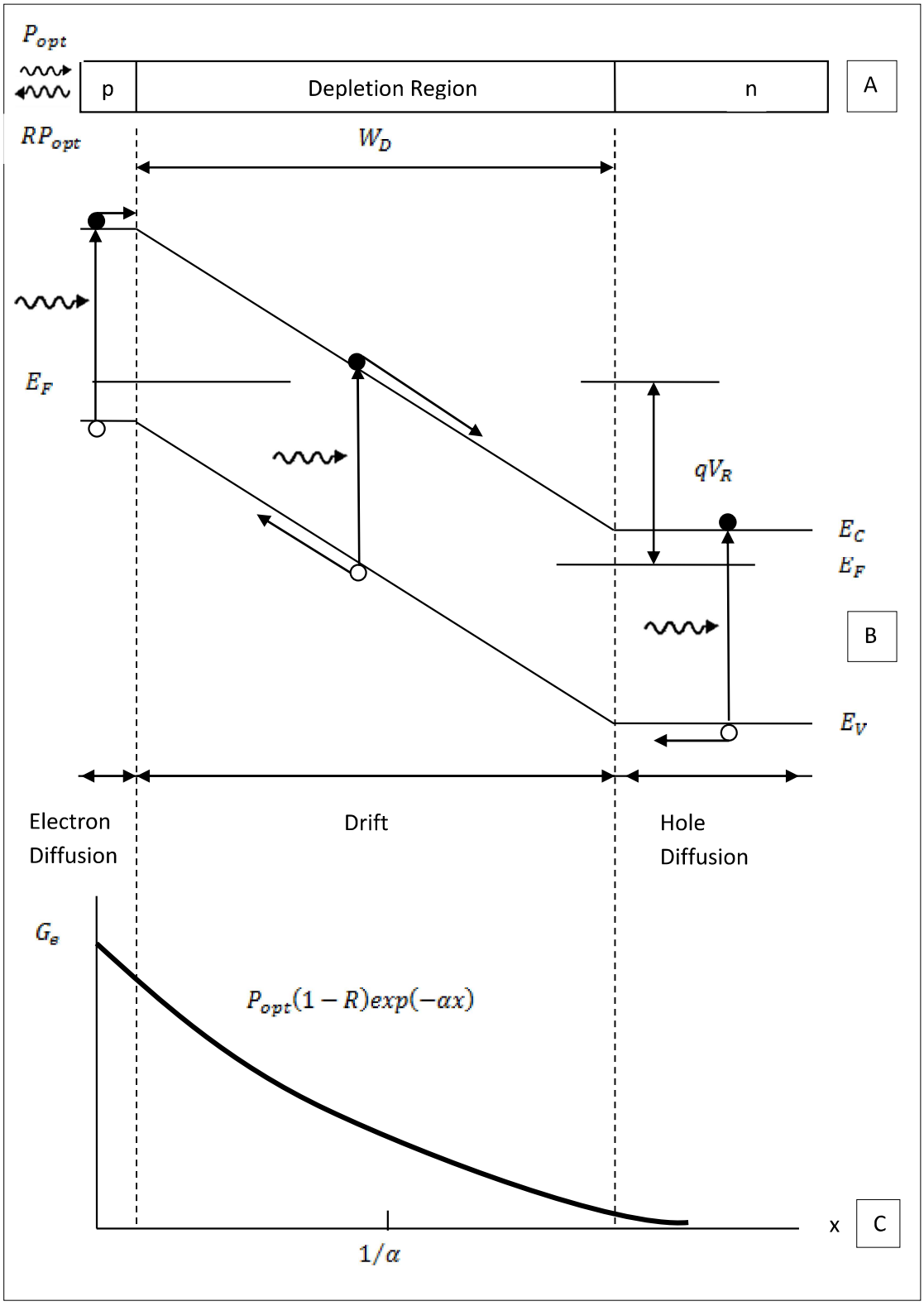

Figure (2.7) Operation of a photodiode : A- Cross sectional view of p-n photodiode, B-Energy band diagram, C-Carrier generation characteristics.

Where D_p is the diffusion coefficient for holes, τ_p is the lifetime of excess carriers, and P_{n0} the equilibrium hole density. The solution of equation (2.31) under the boundary conditions $P_n = P_{n0}$ for $x = \infty$, and $P_n = 0$ for $x = W_D$ is given by:

$$P_n = P_{n0} - [P_{n0} + C_1 exp(-\alpha W_D)] exp\left(\frac{W_D - x}{L_p}\right) + C_1 exp(-\alpha x) \quad \ldots (2.32)$$

With

$$L_p = \sqrt{D_p \tau_p} \quad \ldots (2.33)$$

Where L_p is the diffusion length of holes which is the length over which a hole travels by diffusion before it recombines.

$$C_1 \equiv \left(\frac{\phi_o}{D_p}\right) \frac{\alpha L_p^2}{1 - \alpha^2 L_p^2} \quad \ldots (2.34)$$

The diffusion current density is given by:

$$J_{diffusion} = -qD_p \frac{\partial P_n}{\partial x}|_{x=W_D} \quad \ldots (2.35)$$

$$J_{diffusion} = q\phi_o \frac{\alpha L_p}{1 + \alpha L_p} exp(-\alpha W_D) + \frac{qP_{n0} D_p}{L_p} \quad \ldots (2.36)$$

the total current density is the sum of J_{drift} inside the depletion region and $J_{diffusion}$ outside the depletion region, given by:

$$J_{tot} = q\phi_o \left[1 - \frac{exp(-\alpha W_D)}{1 + \alpha L_p}\right] + \frac{qP_{n0} D_p}{L_p} \quad \ldots (2.37)$$

Under normal operating conditions, the dark-current term involving P_{n0} is much smaller so that the total photocurrent is proportional to the photon flux. The quantum efficiency is:

$$\eta = \frac{A J_{tot}/q}{P_{opt}/h\nu} = (1 - R)\left[1 - \frac{exp(-\alpha W_D)}{1 + \alpha L_p}\right] \quad \ldots (2.38)$$

Qualitatively, the quantum efficiency is reduced from unity due to reflection (R) and light absorbed outside the depletion region. For high quantum efficiency, low reflection (R) and $\alpha W_D \gg 1$ are desirable. However, for $W_D \gg 1/\alpha$, the transit-time delay may be considerable [18].

2.7 GENERAL DIODE RELATIONSHIPS

The built-in potential barrier (V_{bi}) for the p-n junction is given by [24]:

$$V_{bi} = \frac{kT}{q} ln\left(\frac{N_D N_A}{n_i^2}\right) = \frac{q}{2\varepsilon_s}\left(N_D x_n^2 + N_A x_p^2\right) \quad \ldots(2.39)$$

Where $\varepsilon_s = \varepsilon_0 \varepsilon_r$ is the semiconductor dielectric constant.

The number of the negative charges per unit area in the p-region is equal to the number of positive charges in the n-region hence:

$$N_D x_n = N_A x_p \quad \ldots(2.40)$$

By substituting equation (2.40) into equation (2.39) and solving for x_n to obtain the space charge region extended in the n-region given as:

$$x_n = \sqrt{\frac{2\varepsilon_s(V_{bi} + V_R)}{q}\left\{\frac{N_A}{N_D}\left(\frac{1}{N_D + N_A}\right)\right\}} \quad \ldots(2.41)$$

And the space charge region extended in the P-region x_p is given as:

$$x_p = \sqrt{\frac{2\varepsilon_s(V_{bi} + V_R)}{q}\left\{\frac{N_D}{N_A}\left(\frac{1}{N_D + N_A}\right)\right\}} \quad \ldots(2.42)$$

The total depletion or space charge region width W is the sum of the two components given as:

$$W = x_n + x_p = \sqrt{\frac{2\varepsilon_s(V_{bi} + V_R)}{q}\left\{\left(\frac{N_D + N_A}{N_D N_A}\right)\right\}} \quad \ldots(2.43)$$

The maximum electric field at the junction is given by:

$$E_m = -\sqrt{\frac{2q(V_{bi}+V_R)}{\varepsilon_s}\frac{N_D N_A}{N_A+N_D}} \quad \ldots(2.44)$$

Since it have a separation of positive and negative charges in the depletion region, a capacitance is associated with the p-n junction. An increase in the reverse bias voltage dV_R will uncover additional positive charges in the n-region and additional negative charges in the p-region. The depletion layer capacitance is defined as:

$$C_{dep} = dQ/dV_R \quad \ldots(2.45)$$

Where:

$$dQ = qN_D dx_n = qN_A dx_p \quad \ldots(2.46)$$

From equation (2.41) or (2.42), the depletion region capacitance can be written as:

$$C_{dep} = qN_D \frac{dx_n}{dV_R} \quad \ldots(2.47)$$

$$C_{dep} = \sqrt{\frac{q\varepsilon_s N_D N_A}{2(V_{bi}+V_R)(N_D+N_A)}} \quad \ldots(2.48)$$

$$C_{dep} = \frac{\varepsilon_s A}{W} \quad \ldots(2.49)$$

2.8 PHOTODIODE EQUIVALENT CIRCUIT

An equivalent circuit of a photodiode is shown in Figure (2.8).

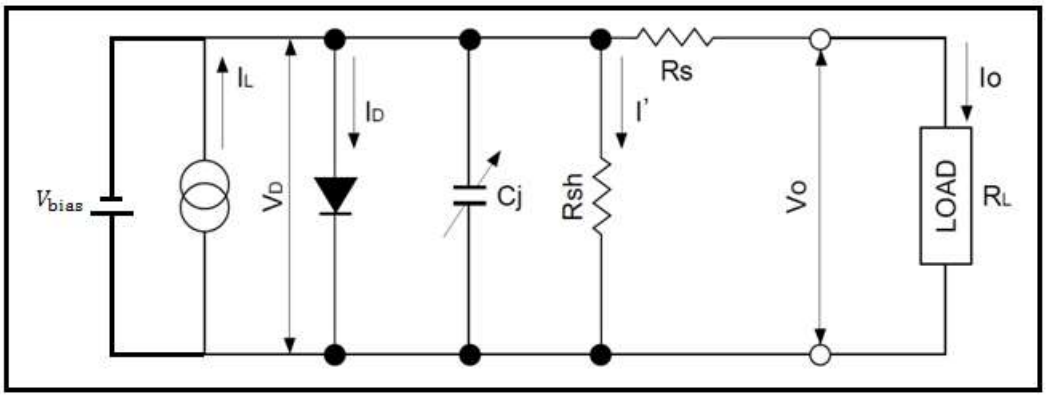

Figure (2.8) Photodiode Equivalent Circuit

Where:

I_L : is the current generated by the incident light (proportional to the amount of light).

I_D : is the diode current.

C_j : is the junction capacitance.

R_{sh}: Shunt resistance.

R_s: Series resistance.

I' : Shunt resistance current.

V_D: Voltage across the diode.

I_0: Output current and,

V_0: Output voltage.

V_{bias}: reverse biasing voltage

Using the above equivalent circuit, the output current I_0 is given as follows:

$$I_0 = I_L - I_D - I' = I_L - I_s\left(exp\frac{qV_D}{kT} - 1\right) - I' \qquad \ldots(2.50)$$

Where:

I_s: is the photodiode reverse saturation current.

q : Electron charge.

k : Boltzmann's constant and,

T : Absolute temperature of the photodiode in ($°Kelvin$).

The open circuit voltage V_{oc} is the output voltage when I_0 equals 0. Thus V_{oc} becomes:

$$V_{oc} = \frac{kT}{q} ln\left(\frac{I_L - I'}{I_s} + 1\right) \quad \ldots(2.51)$$

If I' is negligible, since I_s increases exponentially with respect to ambient temperature, V_{oc} is inversely proportional to the ambient temperature and proportional to the log of I_L. However, this relationship does not hold for very low light levels. The short circuit current I_{sc} is the output current when the load resistance R_L equals 0 and V_0 equals 0, yielding:

$$I_{sc} = I_L - I_s\left(exp\frac{q(I_{sc}R_s)}{kT} - 1\right) - \frac{I_{sc}R_s}{R_{sh}} \quad \ldots(2.52)$$

In the above relationship, the second and third terms limit the linearity of I_{sc}. Since R_s is several ohms and R_{sh} is 10^7 to 10^{11} ohms, these terms become negligible over quite a wide range [19].

2.9 PHOTODETECTOR PARAMETERS

Regardless of the particular type of photodetector employed several device figures of merit help to determine the suitability of a given detector for a specific system application. These figures of merit include:

2.9.1 RESPONSIVITY AND QUANTUM EFFICIENCY

Assume that within a certain observation period t the photodetector has been struck by one photon with the energy $h\nu = hc/\lambda$. Then, the average optical radiation power is $p_{opt} = h\nu/t$. Ideally, this photon produces one electron-hole pair, which after separation supplies into the external circuit one electron with the charge q, and thus the average current is q/t. The coefficient of conversion (the ratio of the output photocurrent (I_p) to the incident optical radiation power (p_{opt})) is called the responsivity of photodetector:

$$S_R(\lambda) = \frac{I_p}{p_{opt}} = \frac{q/t}{h\nu/t} = \frac{q}{h\nu} = \frac{q\lambda}{hc} \qquad \ldots(2.53)$$

Assume now that the ideal photodetector has received N photons within the time t. Then the photocurrent is increased *N*-fold $(I_p = Nq/t)$, and so is the optical radiation power $(p_{opt} = Nh\nu/t)$, but their ratio (responsivity) remains unchanged.

In real photodetectors, however, some of the incident quanta are reflected, some other pass through the crystal without being absorbed, even some of the absorbed quanta are not lucky enough, and the electron-hole pairs generated by them recombine before reaching the junction. So it is only part of the incident quanta, $N' = \eta N$ that produce pairs which are separated in the space charge region and cause photocurrent in the external circuit. Its noted that the photocurrent is only increased by the factor of N' and the expression for the responsivity of real photodetectors contains the coefficient:

$$\eta = \frac{N'}{N} \qquad \ldots (2.54)$$

Is:

$$S_R(\lambda) = \frac{I_p}{p_{opt}} = \frac{N'\,q/t}{N\,h\nu/t} = \frac{N'}{N}\frac{q}{h\nu} = \eta\frac{q\lambda}{hc} \qquad \ldots (2.55)$$

The coefficient η characterizes the performance of photodetector as a counter of quanta of radiation, and is referred to as the quantum efficiency of the photodetector [25].

2.9.2 RESPONSE SPEED

The response speed is limited by a combination of three factors:

1- Drift time in the depletion region.

2- Diffusion of carriers.

3- Capacitance of the depletion region.

Carriers generated outside the depletion region must diffuse to the junction resulting in considerable time delay. To minimize the diffusion effect, the junction should be formed very close to the surface. Most light will be absorbed when the depletion region is sufficiently wide, with sufficient reverse bias the carriers will drift at their saturation velocities. The depletion region must not be too wide, or transit-time effects will limit the frequency response. It also should not be too thin, or excessive capacitance C_j will result in a large $R_L C$ time constant, where R_L is the load resistance [18].

The speed response of a photodetector can be specified either in terms of the frequency-domain or the time-domain response [26].

2.9.2.1 Frequency-Domain Response

When the optical input signal is periodic with fixed amplitude and a frequency *f,* the amplitude of the detector electrical output signal

is not necessarily a constant but may vary with the frequency as shown in Figure (2.9). This phenomenon is usually due to the electrical resistive-capacitance or RC delay of the device. the frequency dependent responsivity can be approximated by:

$$S_R(f) = S_{R_0} \frac{1}{\sqrt{1 + \left(\frac{f}{f_c}\right)^2}} \quad \ldots (2.56)$$

Where S_{R_0} is the responsivity of the photodetector at very low frequencies, and:

$$f_c = \frac{1}{2\pi RC} \quad \ldots (2.57)$$

Where R is the electrical resistance and C is the electrical capacitance of the photodetector [27].

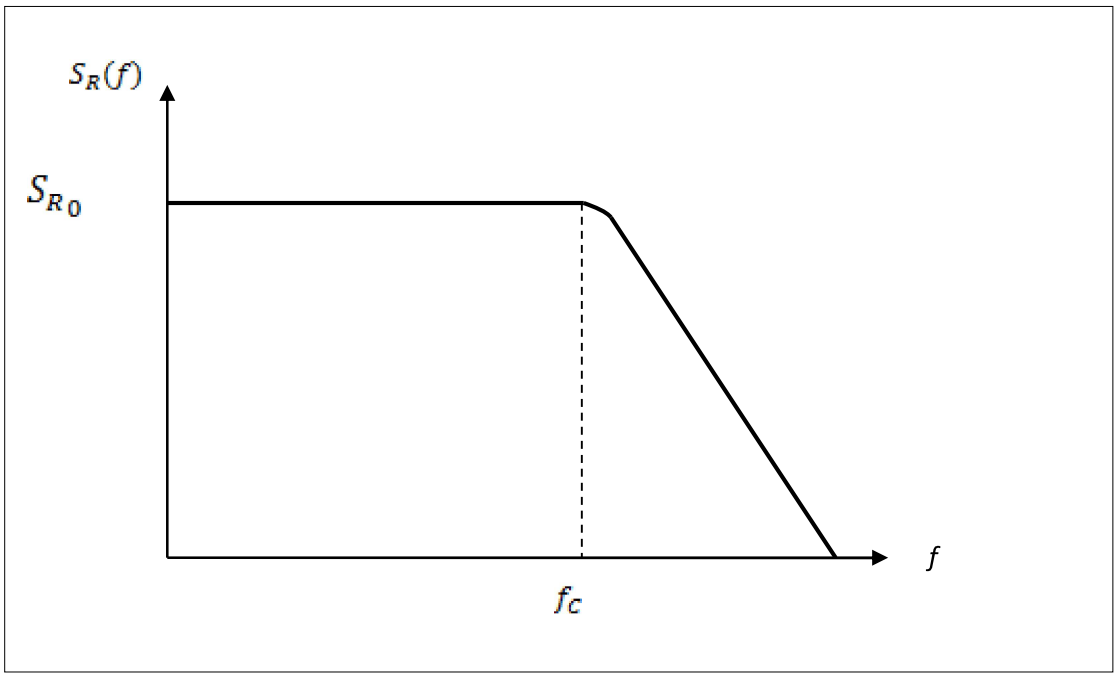

Figure (2.9) Frequency dependent Responsivity

2.9.2.2 TIME-DOMAIN RESPONSE

It is useful to introduce the concept of rise time T_r defined as the time over which the current builds-up from 10 % to 90 % of its final value when the incident optical power is changed abruptly [28]. T_r will depend on the time required for the electrons to travel to the electrical contacts. It will also depend on the response time of the electrical circuit used to process the photocurrent. The rise time of the photodetector can be written by extending the rise time for the RC circuit (where R and C are the resistance and capacitance of the circuit) and is given by:

$$T_r = 2.2(\tau_{RC} + \tau_{tr}) \quad \ldots (2.58)$$

Where τ_{tr} is the transit time and τ_{RC} is the time constant of the equivalent circuit. The transit time is included since time is required before the carriers are collected after their generation through absorption of photons. The maximum collection time is just equal to the time required for an electron to traverse the absorption region. Now, τ_{tr} can be reduced by decreasing space charge width, but that would reduce the quantum efficiency as well.

The bandwidth of the photodetector is determined by the speed with which it responds to variations in the incident optical power. The bandwidth of the photodetector is defined as [28]:

$$\Delta f = \frac{1}{2\pi(\tau_{RC} + \tau_{tr})} \quad \ldots (2.59)$$

Where Δf is the bandwidth of the photodetector, And the relationship between the bandwidth of the photodetector and its rise time is given by [28]:

$$T_r = \frac{0.35}{\Delta f} \quad \ldots (2.60)$$

2.9.3 SIGNAL TO NOISE RATIO (SNR)

The noise is one of the major influencing factors of the detection range. In a photodiode, two sources of noise can be identified, shot noise and Johnson noise [28].

2.9.3.1 SHOT NOISE

Shot noise is related to the statistical fluctuation in both the photocurrent and the dark current. The magnitude of the shot noise is expressed as the root mean square (rms) noise current [28]:

$$I_{sn} = \sqrt{2q(I_p + I_D)f} \quad \ldots(2.61)$$

Where q is the electron charge I_p is the photogenerated current, I_D is the photodetector dark current and f is the noise measurement bandwidth. Shot noise is the dominating source when operating in photoconductive (biased) mode.

2.9.3.2 THERMAL OR JOHNSON NOISE

The shunt resistance in a photodetector has a Johnson noise associated with it. This is due to the thermal generation of carriers. The magnitude of this generated current noise is [28]:

$$I_{jn} = \sqrt{\frac{4K_B T f}{R_{sh}}} \quad \ldots(2.62)$$

Where K_B is the Boltzmann Constant, T is the absolute temperature in degrees kelvin, f is the noise measurement bandwidth and R_{sh} is the shunt resistance of the photodiode. This type of noise is the dominant current noise in photovoltaic (unbiased) operation mode.

All resistors have a Johnson noise associated with them, including the load resistor. This additional noise current is large and adds to the Johnson noise current caused by the photodetector shunt resistance.

2.9.3.3 TOTAL NOISE

The total noise current generated in a photodetector is given by [28]:

$$I_{tn} = \sqrt{{I_{sn}}^2 + {I_{jn}}^2} \quad \ldots(2.63)$$

2.9.3.4 NOISE EQUIVALENT POWER (NEP)

Noise equivalent power is the amount of incident light power on a photodetector, which generates a photocurrent equal to the noise current. NEP is defined as [28]:

$$NEP = \frac{I_{tn}}{S_R(\lambda)} \quad \ldots(2.64)$$

Where $S_R(\lambda)$ is the responsivity in A/W and I_{tn} is the total noise current of the photodetector.

The SNR is usually used to evaluate the performance of a photodetector system. The much broader spectral response of silicon photodetector, although such a broad response is advantageous and even mandatory in some applications, its effect of reducing the

system SNR causes problems for the designer trying to detect a narrow band source in the near IR (such as a LED).

To establish the baseline background measurement, each detector was first tested without powering the LED, the LED was then powered to illuminate the detector and the background measurement was subtracted to determine the signal current. A ratio was established by dividing the signal current by the background light current; this ratio is used to compare between various fabricated photodetectors [29] or by using the equation below:

$$\text{Noise Current Ratio} = (I_{light} - I_{dark})/I_{dark} \quad \ldots(2.65)$$

CHAPTER THREE

PRACTICAL AND SIMULATION TOOLS

3.1 INTRODUCTION

This chapter includes a description about the tools which have been used in the present work to implement and investigate the indium-doped silicon photodetectors, and contains two sections; in the first one a description of the various procedures and tools which have been used to fabricate the photodetectors practically, and in the second one a description of the simulation program (SCAPS) which is used to simulate and analyze the photodetectors.

3.2 THE PRACTICAL SECTION

The system which has been used to fabricate the indium-doped silicon infrared photodetector is the Balzers BA 510 coating unit. It is one of the modern systems for producing thin films for electronic and optical purposes. The materials can be evaporated either by electron beam gun source (E-Gun) or by resistance heating sources (Boats and Coils). Before starting any evaporation process; many preparations should be made such as, cleaning the bell-jar chamber, cleaning the substrate and preparing the masks. The bell-jar chamber and all the installations inside it should be cleaned hardly many times by using cleaning pads and sodium hydroxide solution and usual water.

3.2.1 SILICON WAFER CLEANING

The n-type silicon wafers are used as a substrate to fabricate the indium doped silicon photodetector structure. These wafers have been cut into small pieces by a diamond cutter before any cleaning process. In order to remove the native surface oxide layer and any dirt; the silicon wafers are cleaned by firstly water and acetone and after that the wafers immersed in a hydrofluoric acid (HF) for the sake of

removing the oxide layer on the surface of the silicon wafers. Then, washed with the deionized water, dried with hot air and inserted inside the bell-jar chamber immediately for usage [23].

3.2.2 DEPOSITION OF INDIUM THIN FILM LAYERS

The indium thin film was deposited by using vacuum evaporation technique; indium with purity of 99.95% supplied from Balzers Company was used in the deposition process. Tungsten boat was used as a source of evaporation. The typical evaporation conditions of evaporated indium were as follows:

$\mathrm{TH} = \text{as required}$

$\mathrm{R} = 5\ \mathrm{A}^0/\mathrm{sec}$

$\mathrm{T_s} = 20\ ^\circ\mathrm{C}$

$\mathrm{P} = 10^{-5}\ \mathrm{mbar}$

Where TH is the thickness, R is the rate of deposition, T_s is the substrate temperature, and P is the vacuum pressure. The substrate temperature was held constant at 20 ℃ during evaporation process. The evaporation is stopped as the thickness reaches the required values automatically by the program. After the deposition of the indium film on the silicon wafer, the fabricated cells were heated under vacuum to different temperatures with various periods of time to achieve different cell structures by diffusing the indium to different depths.

3.2.3 DEPOSITION OF ALUMINUM THIN FILMS LAYERS

Aluminum thin films were deposited as a back and front contacts for the fabricated cells by using Balzers coating system. Aluminum material with purity of 99.975% supplied from Balzers Company was used in the deposition process. Tungsten boat was used as a source of evaporation. The typical evaporation conditions of evaporated aluminum were as follows:

$TH = 2000\ A^0$

$R = 5\ A^0/sec$

$T_s = 20\ °C$

$P = 10^{-5}$ mbar

After the deposition of the aluminum film on the rough face of silicon wafer, an aluminum film of 2000 A^0 thick was deposited on the indium doped silicon wafer face using a mask having a specific form, to form the front contact of the cell as shown in figure (3.1).

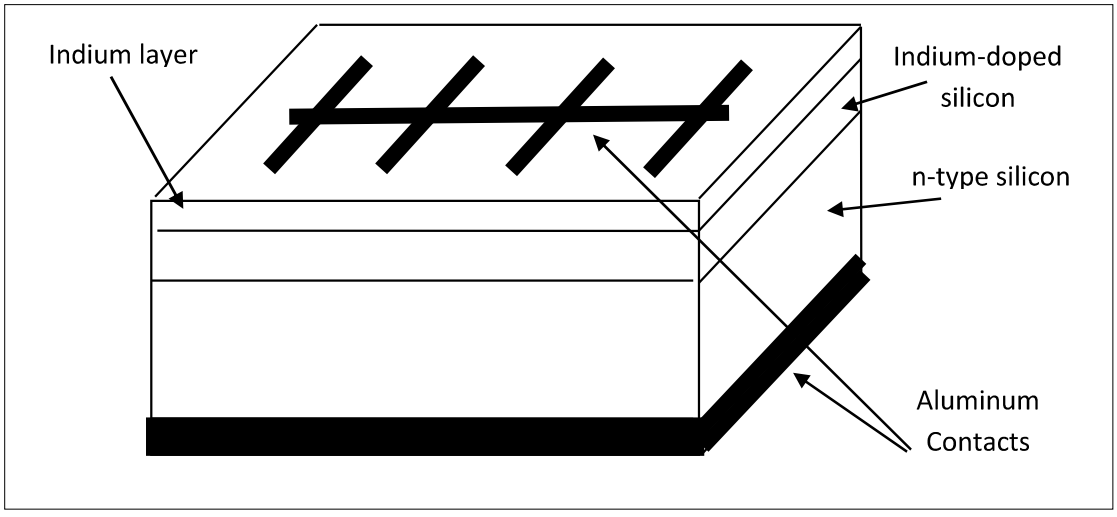

Figure (3.1) the photodiode cell structure after being fabricated.

The fabricated photodetectors were heated under vacuum to a temperature of 350 ℃ for an hour. This heat treatment is necessary to obtain an ohmic contact between the aluminum and the silicon wafers [23].

3.2.4 CURRENT-VOLTAGE (I-V) CHARACTERISTICS

The current-voltage (I-V) characteristics were measured for the fabricated cells under dark without any optical signal, just a voltage source in order to study the conduction mechanism for these cells. A simple electrical circuit is used for the measurement; it composed of a digital multimeter which measures the applied voltage across the sample. This voltage was taken from a stabilized DC power supply which gives a constant DC voltage up to 30 V. The current passing through the sample was measured using an analog ammeter having a current range from 1 μA to 200 mA . The circuit is shown in figure (3.2). There was a mechanical probe which was done in the laboratory to connect the different electrodes of the sample with the measuring units.

3.2.5 SPECTRAL RESPONSE MEASUREMENTS

The spectral response measurements setup used is shown in figure (3.2). The optical part of the spectral response system consists essentially of a light source and optical filters to provide monochromatic light. The wavelength range of interest is from 282.1 nm up to 941.1 nm according to the available filters. The light source consists of a 500 Watt tungsten lamp which placed at a distance away

from the samples to give a specified spectral distribution of the incident light. For example 1.5 AM measures total irradiance of 96.4 m Watt/cm^2. The electrical part of the system consists essentially of a digital ammeter and voltmeter to record the I-V characteristics against light wavelength.

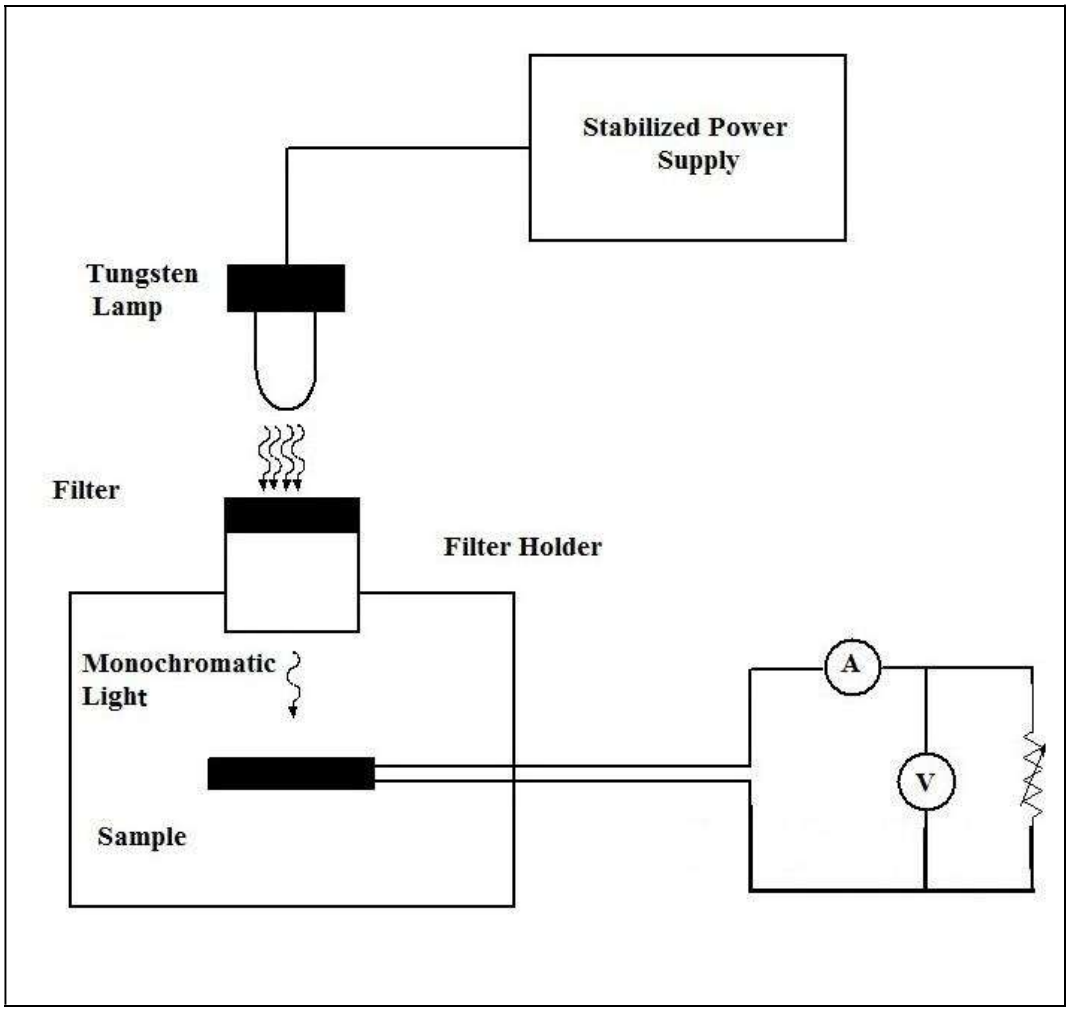

Figure (3.2) The Optical Response Measurement setup

3.3 THE SIMULATION PROGRAM (SCAPS)

SCAPS stands for Solar cell CAPacitance Simulator. In principle, any numerical program capable of solving the basic semiconductor equations could be used for modeling thin film solar

cells. The basic equations are, the Poisson equation, relating the charge to the electrostatic potential ψ, and the continuity equations for electrons and holes, and the electron and hole current density J_n and J_p [30].

Several additional requirements must be met if the program is to simulate thin film polycrystalline heterojunction devices realistically. It must allow for multiple semiconductor layers, at the interfaces between the layers, discontinuities in the energy bands E_c and E_v and hence in the band gap E_g can be present and interface recombination can occur. It should also correctly treat the problem of recombination and charge in deep states in the bulk of the layers. It should be able to calculate and simulate the relevant electro-optical measurements commonly carried out on thin film heterojunctions; this is not only the $\mathrm{I-V}$ characteristics, but also the spectral response $\mathrm{QE}(\lambda)$ and the capacitance measurements $\mathrm{C-V}$ and $\mathrm{C-f}$.

SCAPS is a Windows application program, developed at the University of Gent with Lab Windows/CVI of National Instruments. It has been made available to university researchers in the photovoltaic community after the second PV World Conference in Wien, 1998. A simulation problem is stored in an ASCII file, which can be read and completely edited by the graphical user interface of SCAPS. The program is organized in a number of panels, in which the user can set parameters or in which results are shown. The program opens with an action panel, where the user can set an operating point (temperature, voltage, frequency, illumination), and an action list of calculations to carry out $\left(\mathrm{I-V, C-V, C-f, and\ QE}(\lambda)\right)$ calculations. In each

calculation, the running parameter $(V, f \text{ or } \lambda)$ is varied in the specified range, whilst all other parameters have the value specified in the operation point. One can also load or edit a problem file [30].

3.3.1 THE BASIC SEMICONDUCTOR EQUATIONS

The basic equations for semiconductor device operation describe the static and dynamic behavior of carriers in semiconductors under external influences, such as applied field or optical excitation, that cause deviation from the thermal equilibrium condition. These basic equations are [31]:

3.3.1.1 TRANSPORT EQUATIONS

The most-common current conduction consists of the drift component, caused by the electric field, and the diffusion component, caused by the carrier-concentration gradient. The current-density equations are [31]:

$$J_n = qn\mu_n E + qD_n \frac{\partial n}{\partial x} \quad \ldots(3.1)$$

$$J_p = qp\mu_p E - qD_p \frac{\partial p}{\partial x} \quad \ldots(3.2)$$

3.3.1.2 CONTINUITY EQUATIONS

While the above current-density equations are for steady state conditions, the continuity equations deal with time-dependent phenomena such as low-level injection, generation and recombination. Qualitatively, the net change of carrier concentration is the difference between generation and recombination, plus the net current flowing in and out of the region of interest. The continuity equations are [31]:

$$\frac{\partial J_n}{\partial x} - G(x) + R_n[n(x), p(x)] = -\frac{\partial n}{\partial t} \quad \ldots(3.3)$$

$$\frac{\partial J_p}{\partial x} - G(x) + R_p[n(x), p(x)] = -\frac{\partial p}{\partial t} \quad \ldots (3.4)$$

3.3.1.3 POISSON EQUATION

Which relate the charge to the electrostatic potential ψ [31]:

$$\frac{\partial^2 \psi}{\partial x^2} + \frac{q}{\varepsilon_r \varepsilon_0}[-n(x) + p(x) - N_A^- + N_D^+ + \rho(n,p)] = 0 \quad \ldots (3.5)$$

3.3.2 NUMERICAL PROCEDURES AND ALGORITHMS

SCAPS calculates solutions of the basic semiconductor equations in one dimension and in steady state conditions. These are the Poisson equation for the electrostatic potential ψ, and the continuity equations for electrons and holes, together with the appropriate boundary conditions [32].

3.3.2.1 STEADY-STATE (DC) ANALYSIS

The steady-state semiconductor equations are discretized according to the exponential fitted finite difference scheme and solved by the Gummel iteration scheme. The variations of the variables in one iteration cycle are limited to a user set value (clamping). An own choice of independent variables and a suitable normalization of all variables, were a key issue in obtaining convergence for typical thin film cells at normal working conditions [30].

The simulation domain is partitioned into a number of sub domains. In each sub domain, the differential equations are replaced with algebraic equations, the unknown functions (potential and concentration) are replaced by their values in the node, and finally the set of nonlinear algebraic equations are solved iteratively to find the current at a given applied bias and/or illumination [32].

3.3.2.2 SMALL SIGNAL (AC) ANALYSIS

When a steady state calculation converges, SCAPS can carry out a small signal analysis around the DC operating point, yielding the complex admittance i.e. the capacitance C and the conductance G. This is done by an elegant method, where the coefficient matrix of the equations describing the problem is rearranged such that it forms an (almost) tridiagonal matrix in which each element is in itself a 3×3 matrix. The system is linear and can be solved without iteration for any frequency, provided, of course, that the DC solution is known [30].

The solution of the semiconductor equations in the frequency domain starts from the time dependent semiconductor equations, these equations are discretized in the same way as the steady state equations. The equations in the frequency domain are obtained by linearizing the discretized equations around the DC solution by using first order Taylor series expansion, and by replacing derivatives with respect to time with $j\omega$, where ω is the angular frequency of the AC excitation. After linearization of the Poisson equation and the continuity equations, one obtains a linear system of *3N* equations with *3N* variables, for the solution of this system; a Gummel-like iteration method is commonly used.

However, as this system is linear, the solution can be found in just one step proposed in [32] to minimize the required calculation time. From the small signal amplitudes of the potential and the concentrations, the small signal amplitude $\tilde{J}$ of the total current density is calculated. Finally, the capacitance and conductance are given by:

$$G(\omega) = Re\left(\frac{\tilde{J}}{\tilde{V}}\right) \qquad \ldots(3.6)$$

$$C(\omega) = \frac{1}{\omega} Im\left(\frac{\tilde{J}}{\tilde{V}}\right) \quad \ldots (3.7)$$

Where $\tilde{V}$ is the small signal amplitude of the applied bias, (the AC voltage) [32].

3.3.3 PHYSICAL MODELS INCLUDED IN SCAPS

As stated previously, several requirements must be met if the program is to simulate thin film polycrystalline heterojunction devices realistically. Now, a discussion on how these features are implemented in SCAPS will be done.

3.3.3.1 DEEP BULK LEVELS

In each layer, the type (donor or acceptor) and density of one shallow level can be defined; it is completely ionized and does not contribute to recombination. Also, up to three deep levels can be defined. Recombination in these levels and their occupation is described by the Shockley-Read-Hall (SRH) formalism, and charge is defined by the occupation of the level and its type (donor or acceptor, or neutral (i.e. a hypothetical center carrying no charge)). The levels can be energetically distributed in the forbidden zone (single level, uniform band, Gauβ, or exponential tail). The concentration of the shallow or deep states can vary spatially (uniform, step, linear or exponential) [30].

3.3.3.2 INTERFACE STATES AND BAND DISCONTINUITIES

The quasi-Fermi levels are allowed to be discontinuous at the interfaces. To handle this mathematically, an extra node at each interface is introduced in the discretization. The relation between Fermi level discontinuity, carrier concentrations and current is given by the expressions for thermionic current at the interface [30] [33].

Recombination at the interface states is modeled by the Pauwels-Vanhoutte theory. This theory is an extension of the classical Shockley-Read-Hall formalism for recombination in the bulk. According to this model, the interface states communicate with four bands instead of two (classical theory), this means the conduction and valence bands of both semiconductors at the interface. The occupation probability of the interface states is therefore determined by four concentrations instead of two.

The interface states are characterized by a surface density, an energy level and four capture cross sections. In SCAPS program, the interface states can be distributed in energy, in the same way as the bulk states. At the metal-semiconductor interfaces (contacts), transport of majority carriers is described by thermionic emission (Bethe theory). Transport of minority carriers is described by their surface recombination velocity S_n or S_p at the contact [32].

3.3.3.3 GRADED STRUCTURES

It should be noted that by implementing a graded composition of the cell layers, not only the band gap $E_g(x)$, but almost all other materials properties become graded: electron affinity $\chi(x)$, optical absorption $\alpha(\lambda,x)$, effective density of states $N_c(x)$ and $N_v(x)$, doping density $N_D(x)$ and $N_A(x)$, transport properties $\mu_n(x)$ and $\mu_p(x)$, recombination properties $N_t(x)$, $\sigma_n(x)$, $\sigma_p(x)$,etc. A simulation tool including grading thus should take everywhere the position dependent value of the materials parameters. It is not trivial at all to implement this in a way that is convenient for the user and efficient for the internal operation of the program. A more scientific

consequence of grading is that it is modifying the semiconductor equations governing the problem.

In a problem with uniform layers, the driving forces for electrical current are the electrostatic potential gradient $\nabla\psi$ (drift current) and the concentration gradients ∇n and ∇p (diffusion current). When grading is present, extra driving terms should be added, the gradient of the electron affinity $\nabla\chi$, the gradient of the band gap ∇E_g, and the gradients of the effective density of states in the conduction and valence bands: $\nabla(logN_c)$ and $\nabla(logN_v)$. Also, the electron and hole continuity equations are modified by the presence of a mobility gradient $\nabla\mu_n$ or $\nabla\mu_p$, and the Poisson equation is modified by a gradient ∇ε in dielectric constant.

These modified equations have to give a suitable and materials oriented description of the grading of the various materials parameters, it has chosen to derive all parameters consistently from the composition grading of a layer. Each layer is assumed to have composition $A_{1-y}B_y$. The user defines the properties of the pure compounds A (e.g. A =$CuInSe_2$) and B (e.g. B = $CuInS_2$), and the composition grading y(x) over the thickness of the layer thus defining the composition values y at the left and right side of the layer, and by specifying some grading law in between. All materials properties P are then derived from the local composition parameter y(x), that is, P[y(x)] is evaluated.

Several grading laws are implemented in SCAPS and offered by the user interface: linear, logarithmic, parabolic, power law, exponential, effective medium and a Beta function. These grading laws can be used to set the composition grading y(x) over a layer, as

well as to set the composition dependence P(y) of a property. The following properties can be graded in SCAPS: E_g, χ, ε, N_c, N_v, μ_n, μ_p, v_{thn}, v_{thp}, $N_D(x)$, $N_A(x)$, $N_t(x)$ and $\alpha(\lambda, x)$ [34].

3.3.3.4 INTRA-BAND TUNNELING

For heterojunction devices with a spike in one of the bands at the junction, intra-band tunneling will enhance the current through the interface. Adding a model for intra-band tunneling to SCAPS allows to correctly simulate the current transport properties of a heterointerface. Tunneling of electrons through a potential barrier is a quantum mechanical phenomenon. To describe it correctly, one should write down the Schrödinger equation for electrons with energy below the barrier tip.

This gives a differential equation which can be solved in principal and would result in electron wave vectors, from which the tunnel probability can be calculated. However, the numerical solution is not straightforward and requires great computational power. As is the habit in such a case, one will therefore use the Wentzel-Kramers-Brillouin (WKB) approximation for the tunneling probability [33].

3.3.3.5 ABSORPTION IN THE SEMICONDUCTOR LAYERS

An exponential absorption law is assumed for all semiconductor layers. The absorption characteristics can be also taken from a user defined file [31].

3.3.3.6 OPTICAL LAYERS

There is a new possibility to introduce optical layers at both back and front contacts. These layers only act as optical filters for the incoming light. At both contacts, the filter specified can be used as transmission or reflection spectrum [2].

3.3.3.7 OPTICAL GENERATION

SCAPS can handle steady state illumination by monochromatic light or by light of a standard spectrum (AM1.5G and AM1.5D are implemented by default). The wavelength region can be limited to simulate the use of long pass and short pass filters. Above that, a small signal illumination can be added to simulate a spectral response measurement [30].

3.3.3.8 QUANTUM EFFICIENCY CALCULATION

In SCAPS, quantum efficiency is calculated by calculating two times the current density, once in the working point at the given bias voltage and bias illumination, and once in the working point conditions with a number of monochromatic photons superimposed to the spectrum, both values are subtracted and presented as quantum efficiency [31].

3.3.3.9 EXTERNAL NETWORK ELEMENTS

In order to be able to simulate the influence of series and shunt resistances to devices characteristics, the adding of such resistances to the problem as an external element is implemented in SCAPS. The implementation of this option was inspired by the need for external resistances with transient analysis [31].

CHAPTER FOUR

SIMULATION RESULTS AND DISCUSSION

4.1 INTRODUCTION

The SCAPS program has been used to investigate the various device parameters on the quantum efficiency of the photodetector, the quantum efficiency here represents the spectral response of the photodetector.

Using SCAPS, the silicon p-n junction photodiode structure can be built and one can change various parameters and take the quantum efficiency (η) versus wavelength (λ) curve correspondingly.

4.2 EFFECT OF INDIUM CONCENTRATION ON THE QUANTUM EFFICIENCY

Fig (4.1) represents the quantum efficiency dependence on the incident radiation wavelength at different Indium concentration. The quantum efficiency (η) depends upon the photocurrent and the photon energy according to equation (2.55) the quantum efficiency is the number of electron-hole pairs generated for each incident photon, therefore, the explanation of the effect of λ on photocurrent can be used here to interpret the effect of λ on the quantum efficiency.

As shown in figure (4.1), the quantum efficiency increases when the indium concentration increases, the reason for this increase is mainly because the increase of the electric field in the depletion region, where the electric field increases with the increase of indium concentration according to equation (2.44), which causes more photogenerated charge carriers to contribute in the generation of photocurrent. When the indium concentration is below the background concentration of shallow donors by a significant amount, the quantum efficiency of the photodiode is similar to that of a piece of silicon with

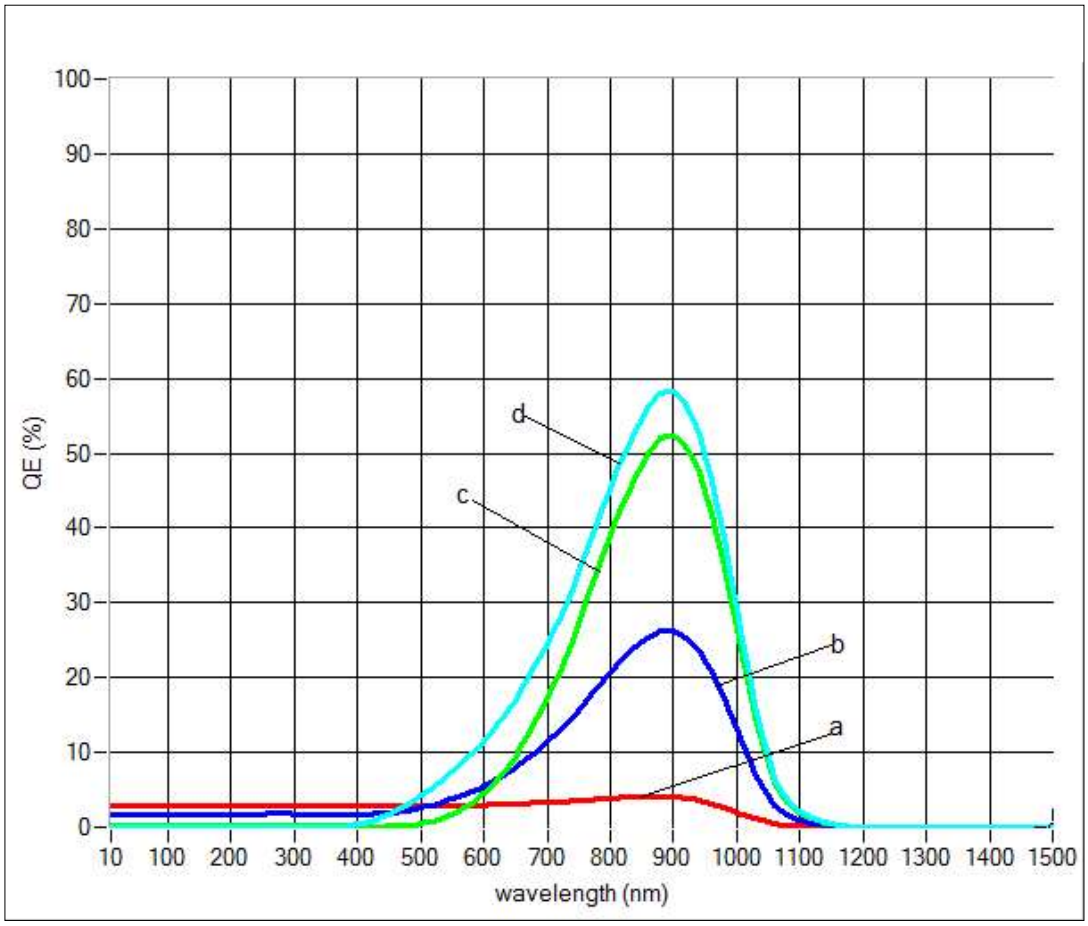

Figure (4.1) the effect of indium concentration change: a- 1×10^{13} , b-8×10^{13} , c- 1×10^{14} , d- $1 \times 10^{18}/\mathrm{cm}^3$. With background concentration equal to 1×10^{14} and $\mathrm{Th_n} = 100\mu\mathrm{m}$, $\mathrm{Th_p} = 20\mu\mathrm{m}$.

shallow impurities, because there is no depletion region formed yet. Where, the response to light is the generation of e-h pairs, the generation process is governed by the absorption mechanism in silicon which is spectrally dependent, after the generation of e-h pairs, there is a carrier gradient which causes a diffusion current, and in this case, the quantum efficiency will decrease with the increase of sample length because of the carriers lifetime or in other words the diffusion

length is small compared to the length of the sample so that most of photogenerated carriers will recombine before crossing the sample and contribute in photocurrent.

The increase of indium concentration will increase the absorption coefficient of electron photoemission from the impurity level and also the absorption coefficient of holes photoemission from the impurity level, as indicated by equations (2.5 and 2.6), this increment in the total absorption coefficient (equation (2.4)) is responsible partially in the increment of quantum efficiency when indium concentration increases according to equation (2.3).

4.3 THE EFFECT OF JUNCTION DEPTH ON THE QUANTUM EFFICIENCY

Figures (4.2) and (4.3) represent the quantum efficiency dependence on the incident radiation wavelength at different junction depths and impurity concentrations. From the figures below, at each junction depth there is a wavelength at which maximum quantum efficiency ($\eta_{\max}$) occurs, no matter how much the concentration. This ($\eta_{\max}$) is due to maximum carrier collection in the depletion region at that wavelength.

For each impurity concentration, there is a junction depth at which maximum $\eta_{\max}$ occurs, from figures (4.2) and (4.3) the junction depths at which maximum $\eta_{\max}$ are 20 µm for indium concentration10^{14}, and 5 µm for indium concentration10^{16}. It's noted that as the indium concentration increases, the junction depth at which maximum $\eta_{\max}$ occur decreases, and also maximum $\eta_{\max}$ increases.

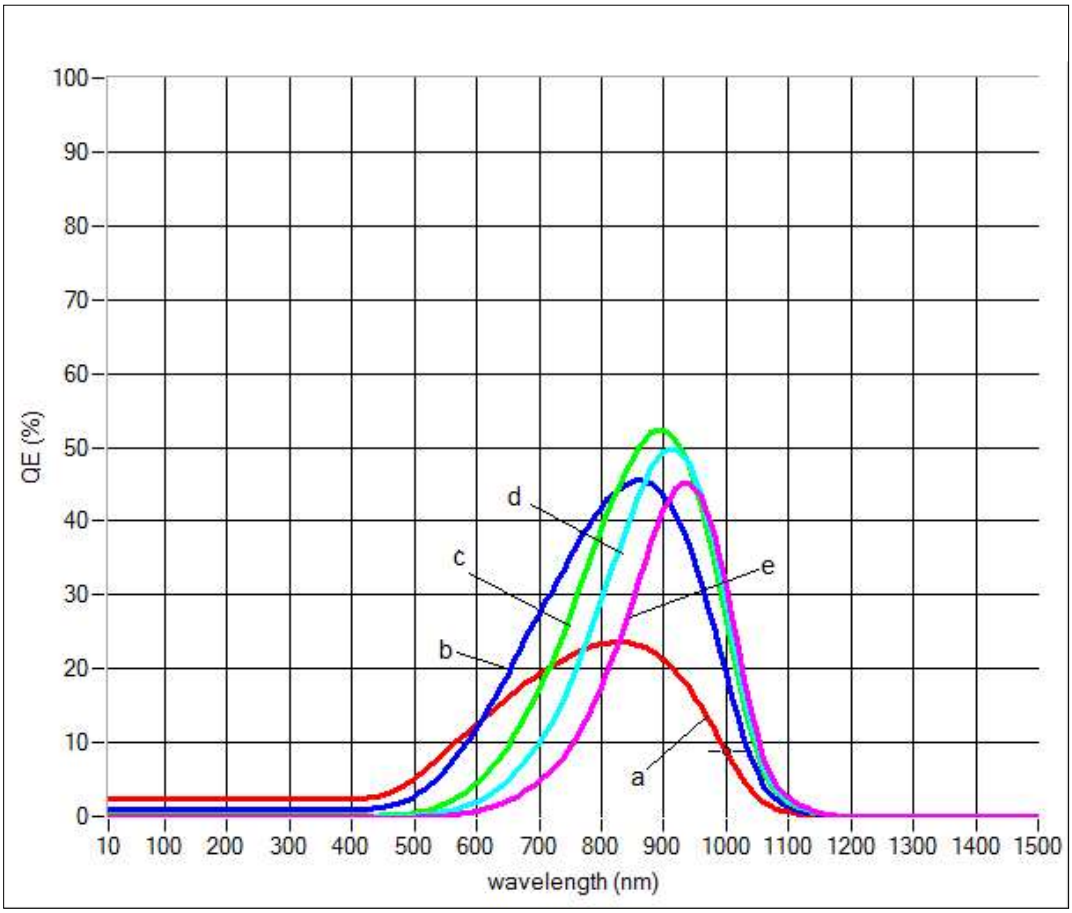

From equation (2.43) as the doping concentration increases, the depletion region width decreases and E_{max} increases and according to

Figure (4.2) effect of Junction depth change a- $5\mu m$,b- $10\ \mu m$,c- $20\mu m$,d- $30\mu m$,e- $50\mu m$.with background and indium concentration equal to 10^{14} and $\mathrm{Th_n} = 100\mu m$.

equations (2.16 and 2.17) the carriers lifetime (which is the time over which the photogenerated carriers become free) decreases, so in order to maximize the quantum efficiency to maximum η_{max} then it must bring the depletion region closer to the surface in order to achieve maximum carrier collection in the depletion region. Therefore, due to

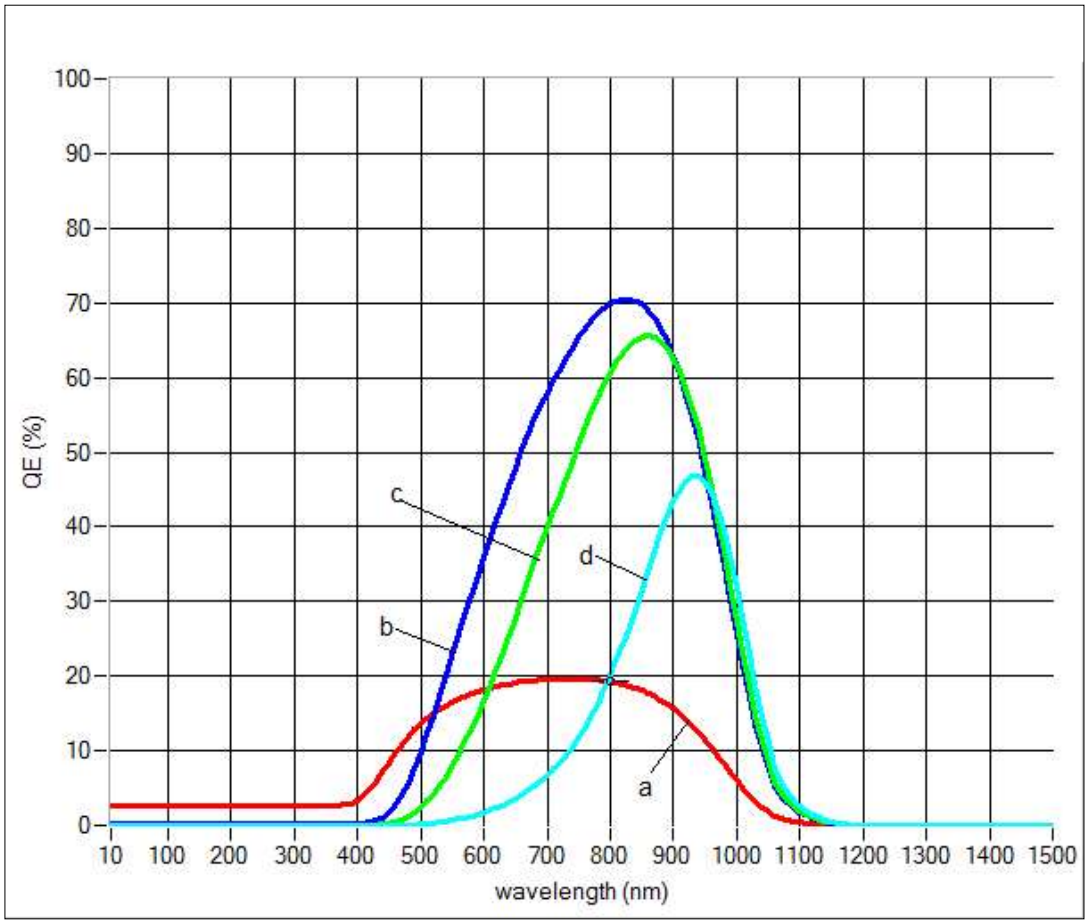

bringing of depletion region closer to the surface and the increment in the absorption coefficient due to the increase of indium concentration then the photocurrent and hence the quantum efficiency will increase.

Figure (4.3): Junction depth change with a- 1 μm, b- 5 μm, c- 10 μm, d- 50 μm. With background and indium concentration equal to 10^{16} and $Th_n = 100\mu m$.

By observing figures (4.2) and (4.3), it can be noted that, by increasing the junction depth, the spectral response range decreases, where the spectral response range is the range of wavelengths over which there is a significant quantum efficiency values. The reason of this decrement is because of, as the junction depth increases, the shorter wavelengths generate carriers in a region which is far from the

depletion region and near the surface, so that the time required to reach the depletion region is larger than the carrier lifetime, therefore they recombine before reaching the depletion region. Therefore, the response will move toward the longer wavelengths. From the other side, when the wavelength exceeds the long cutoff wavelength, decided by minimum energy required by the impurity photovoltaic effect (IPV) to put the carriers in the conduction state, the response falls rapidly to zero. Therefore, the spectral response range decreases while junction depth increases.

To get a high speed response in a photodiode, then it must make the generation process of electron-hole pairs to take place mostly in the depletion region to avoid the delay associated with the crossing of the diffusion region outside the depletion region by the generated carriers produced in those regions. Therefore, it's expected that the response speed and hence the frequency response will be worse as the junction depth increases.

4.4 EFFECT OF DOPING LEVEL IN THE n-REGION ON THE QUANTUM EFFICIENCY OF PHOTODIODE

Figure (4.4) shows the effect of changing the doping level of the n-region on the quantum efficiency. From the figure, it has been shown that the increase in doping level results in the increase of quantum efficiency because of more potential difference will exist in the depletion region, as stated previously in the discussion on the quantum efficiency dependence on indium concentration, and therefore the photogenerated current will be more.

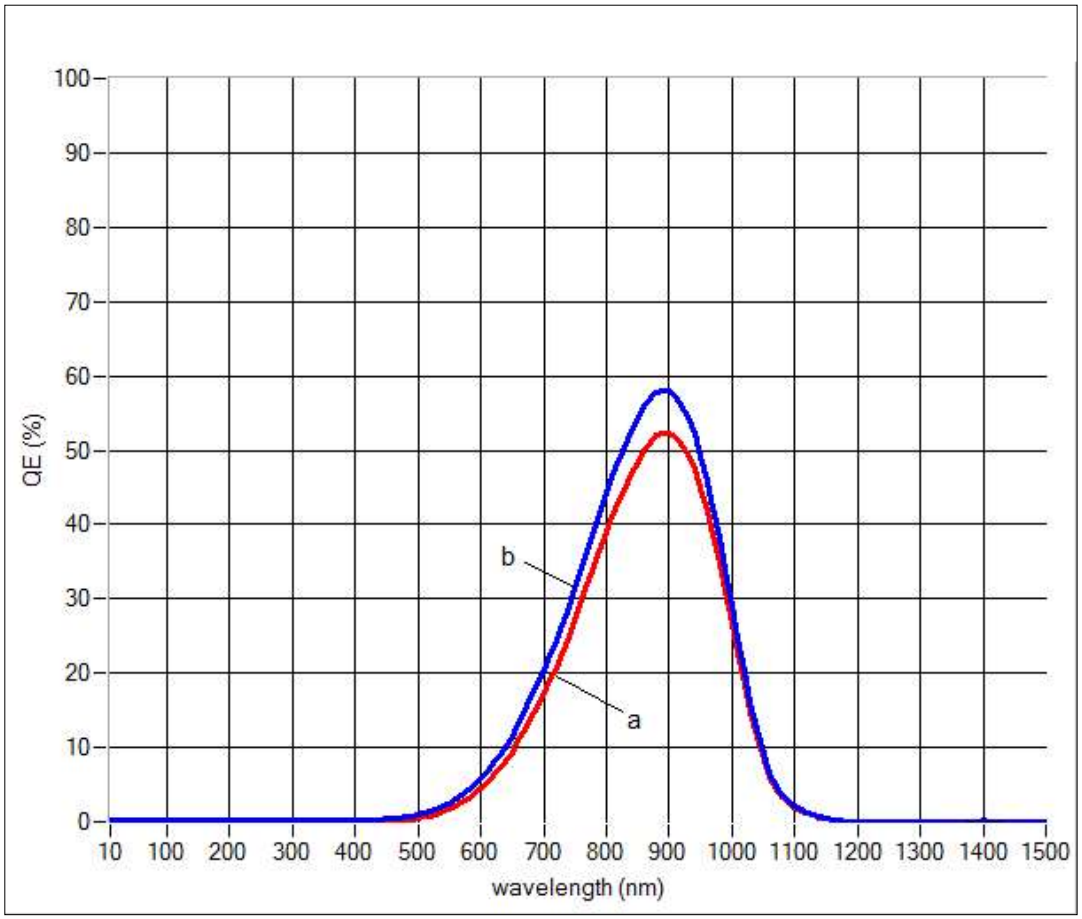

Figure (4.4) the effect of n-type concentration change a- 1×10^{14}, b- $1 \times 10^{16}/cm^3$. With n_p dopant 10^{14} and indium concentration 10^{14}, $Th_n = 100\mu m\,, Th_p = 20\mu m\,.$

4.5 EFFECT OF n-REGION LENGTH ON THE QUANTUM EFFICIENCY

Figure (4.5) shows that while the n-region length increases, this increment results in rising the quantum efficiency curves to a higher levels especially from the long wavelengths side around 0.9 μm and above, hence widening the spectral response range, this is because of while the n-region length becomes longer, the long wavelength will

take the chance to generate more carriers, that is because of at longer wavelengths the photodiode has a very small absorption coefficient which means longer region to the absorption process to take place, and now because of more carriers generated then, after they diffuse to the depletion region they will contribute in photocurrent generation. As stated before the more the carriers generated outside the depletion

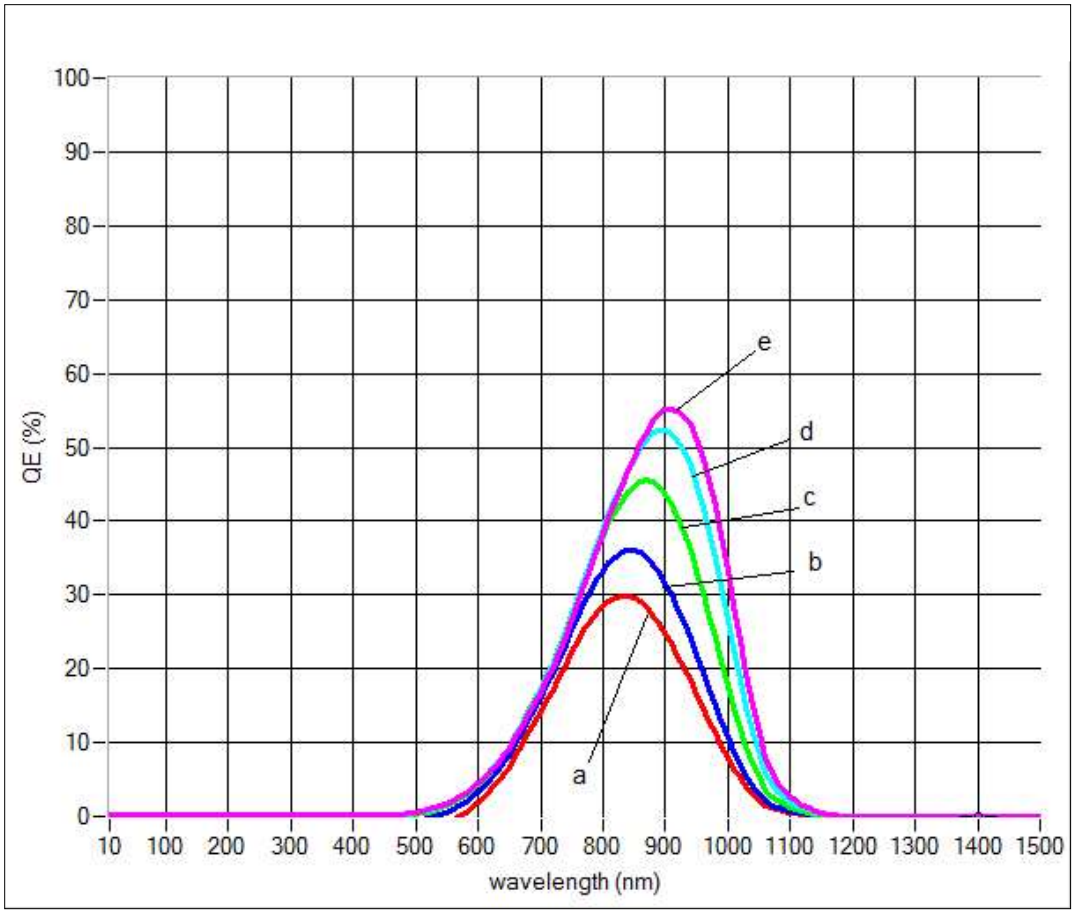

region means more delay and the increase in quantum efficiency opposited by the decrease in response speed.

Figure (4.5) the effect of n-region length change a- 10μm, b- 20 μm, c- 50 μm,d- 100 μm,e- 150 μm. With background and indium concentration equal to 10^{14} and $Th_p = 20\mu m$.

4.6 THE EFFECT OF p-REGION DOPANT TYPE ON THE QUANTUM EFFICIENCY

In figure (4.6) there is a comparison between two types of p-type dopants in the p-region, one is indium and the other is shallow acceptor dopants, and their effects on the quantum efficiency of the photodiode. It's noted that with the indium as a doping material, the photodiode has a narrower spectral response range and smaller quantum efficiency. The adding of a deep acceptor dopant like indium in silicon will introduce an efficient generation-recombination centers in the silicon, and by increasing the concentration of indium this will increase these centers number.

According to equations (2.16 and 2.17), as the concentration of indium increases, the lifetime of electrons and holes photogenerated in the photodiode will decrease, which means that, at a certain photodiode length and radiation wavelength, the photogenerated carriers that reach the depletion region will decrease because of the increased recombination rate as the indium concentration increases. The replacement of indium by a shallow acceptor means that the photodiode will have a longer lifetime because of the shallow dopants represents an inefficient generation-recombination center. Even with no shallow acceptor, just pure silicon, the lifetime will be longer and more carriers will reach the depletion region and larger quantum efficiency at shorter wavelengths.

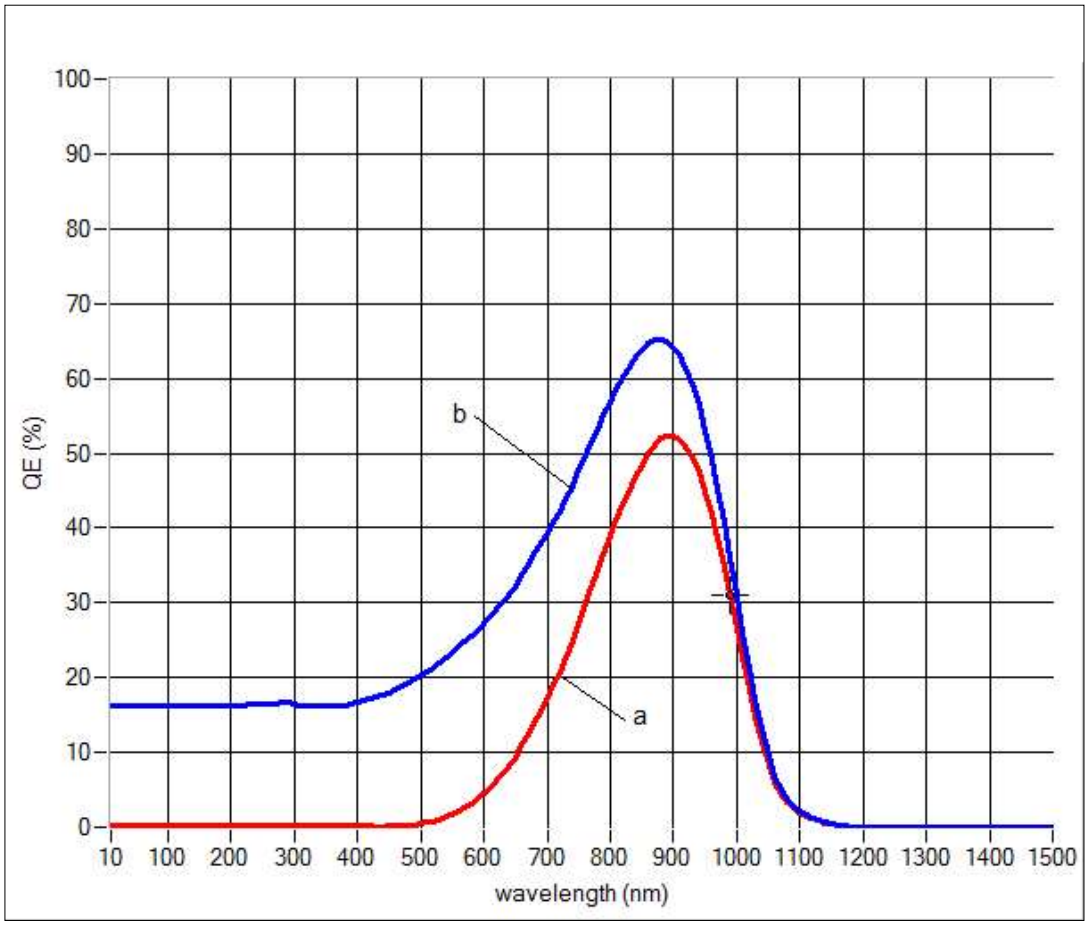

Figure (4.6) a- Mid-deep level (indium) dopant, b- shallow-level dopant. In p-region silicon with $\mathrm{Th_n} = 100\mu\mathrm{m}, \mathrm{Th_p} = 20\mu\mathrm{m}$ and background concentration10^{14}.

CHAPTER FIVE

PRACTICAL RESULTS AND DISCUSSION

5.1 INTRODUCTION

This chapter includes a brief description of a practically worked photodiode by using a vacuum evaporation technique, followed by an electrical characterization of the fabricated photodiode, and by using the optical response measurement setup of chapter three, the spectral and optical response measurements are implemented, and the spectral characteristics of the fabricated photodiode were obtained and discussed. In the remaining of the chapter, an overview to various attempts worked throughout the preparation of this thesis to achieve photodiodes practically by using the vacuum evaporation technique.

5.2 THE PRACTICAL WORK

As stated before, the Balzers BA 510 coating unit is used to fabricate the photodiode. The indium doped silicon layer was implemented with the following conditions:

Th = 500 $A°$

R = 5 $A°/sec$

$T_s = 20$ ℃

P = 2×10^{-4} mbar

Annealing temperature = 350 ℃

Annealing period = one hour

And the aluminum front and back contact layers were implemented after, with the following conditions:

Th = 2000 $A°$

R = 5 $A°/sec$

$T_s = 20$ ℃

P = 4×10^{-4} mbar

Annealing temperature = 350 ℃

Annealing period = one hour

Figure (5.1) shows a block diagram of the fabricated photodiode.

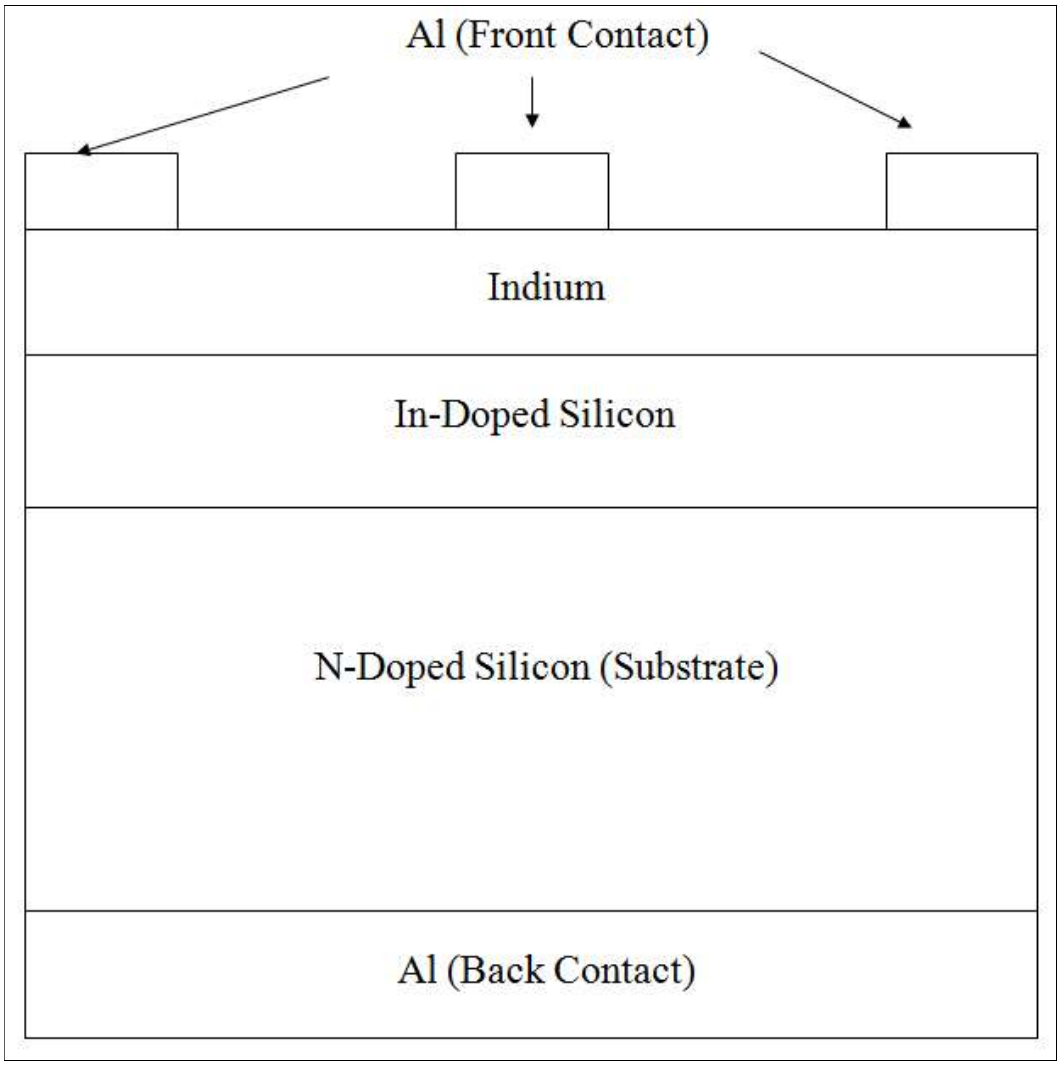

Figure (5.1) photodiode Block Diagram

5.3 THE ELECTRICAL CHARACTERISTICS OF THE FABRICATED PHOTODIODE

Figure (5.2) shows the I-V characteristics of the fabricated photodiode under dark. It is found that the dark forward current starts increasing exponentially at 0.4 volt; this indicates the exponential dependence of the current on voltage which can be written as:

$$I = I_0 \exp\left(\frac{V}{n_f KT}\right) \quad \ldots(4.1)$$

Where I_0 is the reverse saturation current, and n_f is the diode ideality factor which is considered as a measure of the quality of the junction. The photodiode has a high leakage current, because the depletion region is narrow and the junction depth is very small.

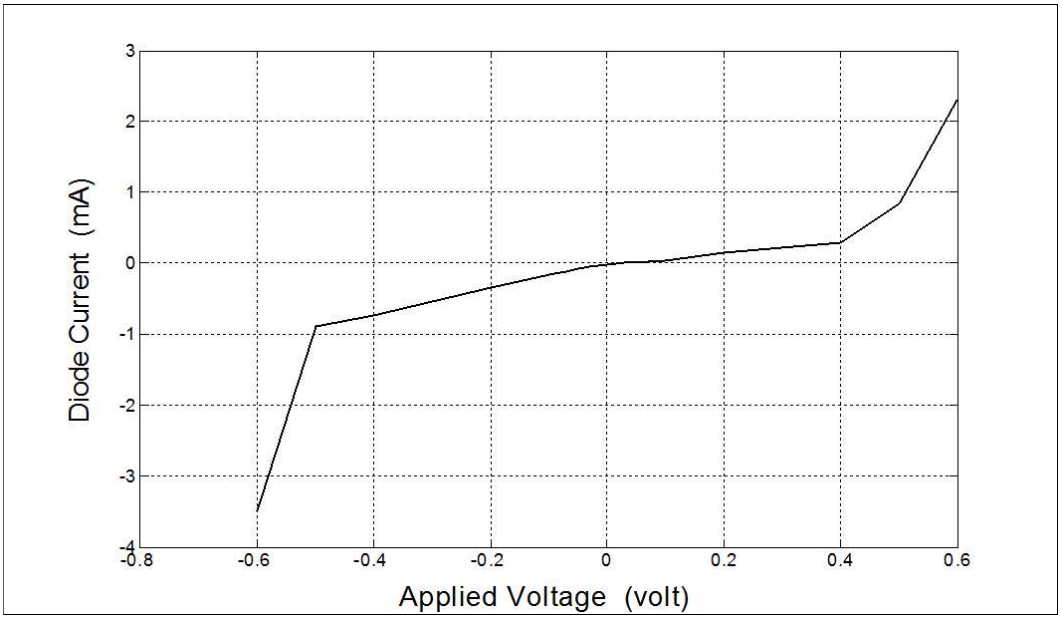

Figure (5.2) I-V characteristics of the fabricated photodiode

5.4 THE SPECTRAL RESPONSE OF INDIUM-DOPED SILICON PHOTODIODE

Figure (5.3) shows the current response of indium-doped silicon photodiode. The short circuit current was measured at 4000 lux and found that the maximum current can be equal to 6 μA at 941.1 nm wavelength. It is clear that at the junction depth formed, the electron-hole pairs generated are almost collected inside the junction yielding a maximum current generation.

From figure (5.3), there is no photoresponse of the photodiode at wavelengths less than 450 nm. This can be attributed to the high absorption coefficients at these wavelengths so that all generation-recombination processes take place near the surface and the generated electron-hole pairs recombine before reach the depletion layer.

The current starts increasing at $\lambda > 450$ nm and the maximum current obtained at wavelength 941.1 nm. This can be explained by the fact that at this region of photoresponse, the two semiconducting layers of the photodiode (n-type silicon and p-type indium-doped silicon) and the depletion layer contribute in the photogeneration of the electron-hole pairs.

As λ increases above 941.1 nm; the current starts decreasing gradually, the current generation at this range can be attributed to the fact that at this range of wavelengths most of the generated electron-hole pairs are generated due to subgap absorption mechanism (IPV effect) which extend the photodiode response up to 1100 nm or more, the energy of the photons of the light which have wavelength longer than 1100 nm are so small such that there is no enough energy capable

of lifting the electrons to conduction band and hence no photoresponse.

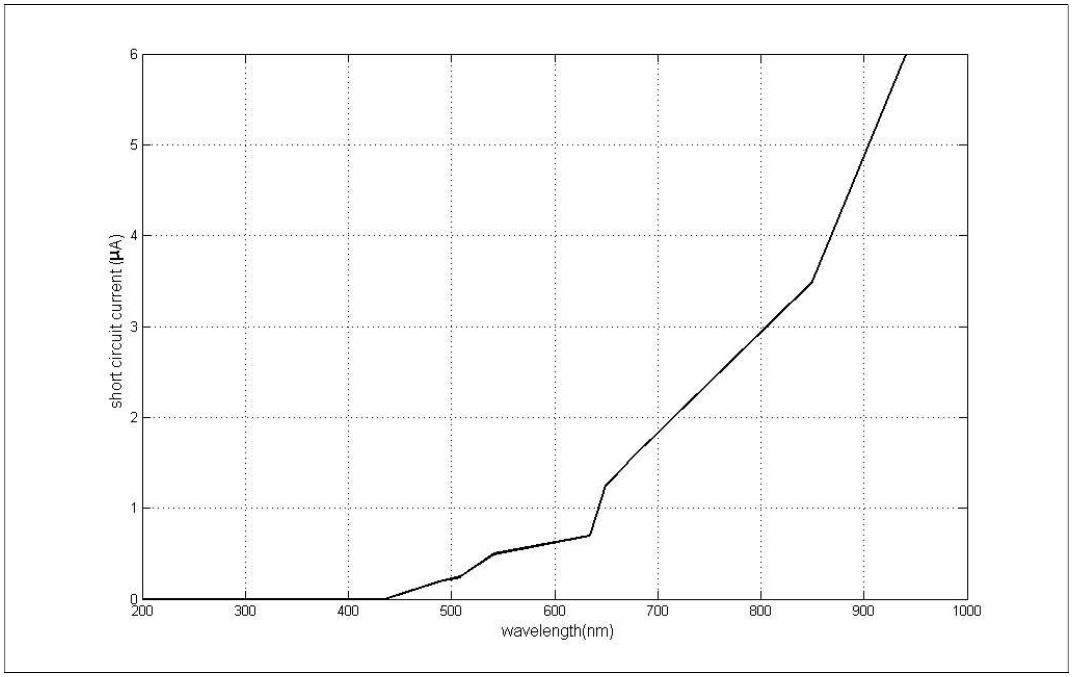

Figure (5.3): current spectral response

Figure (5.4) shows the relative spectral responsivity of the fabricated photodiode. As stated before the responsivity is the ratio of the photocurrent to the incident optical power. And figure (5.5) shows the relative quantum efficiency of the fabricated photodiode. The quantum efficiency is related to the spectral responsivity by equation (2.55) it is simply related to responsivity ($S_R(\lambda)$) by some physical constants ($hc/q = 1240$) and the free-space wavelength (λ) in (nm).

The effect of wavelength on the photocurrent response can be used to interpret the effect of wavelength on the quantum efficiency and responsivity which was discussed previously.

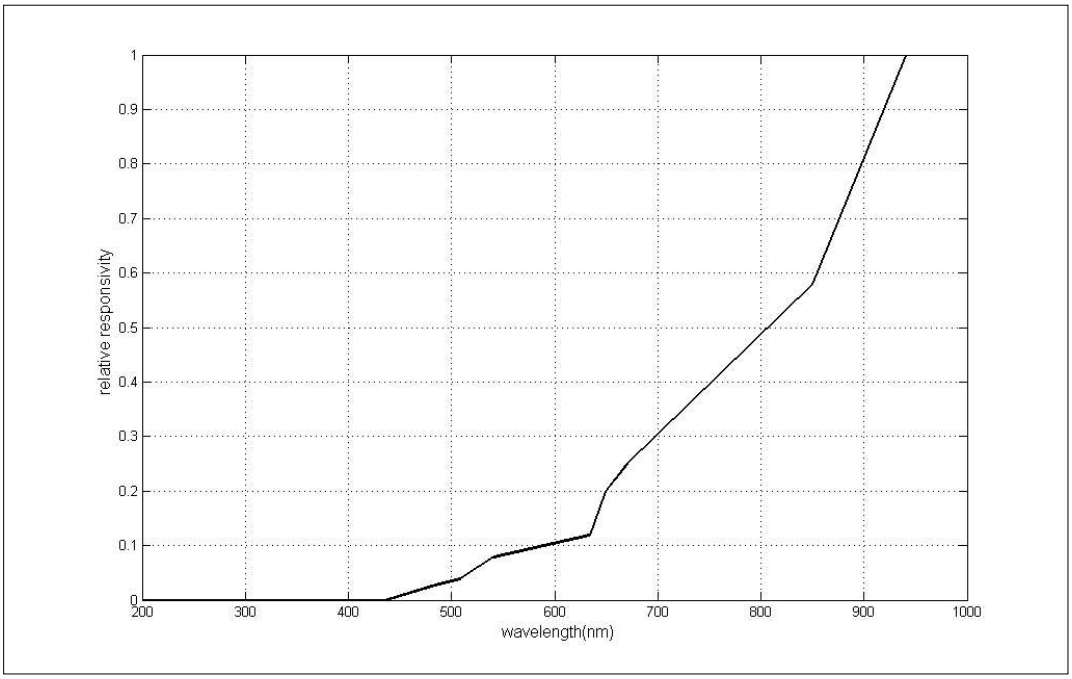

Figure (5.4): photodetector relative responsivity versus wavelength

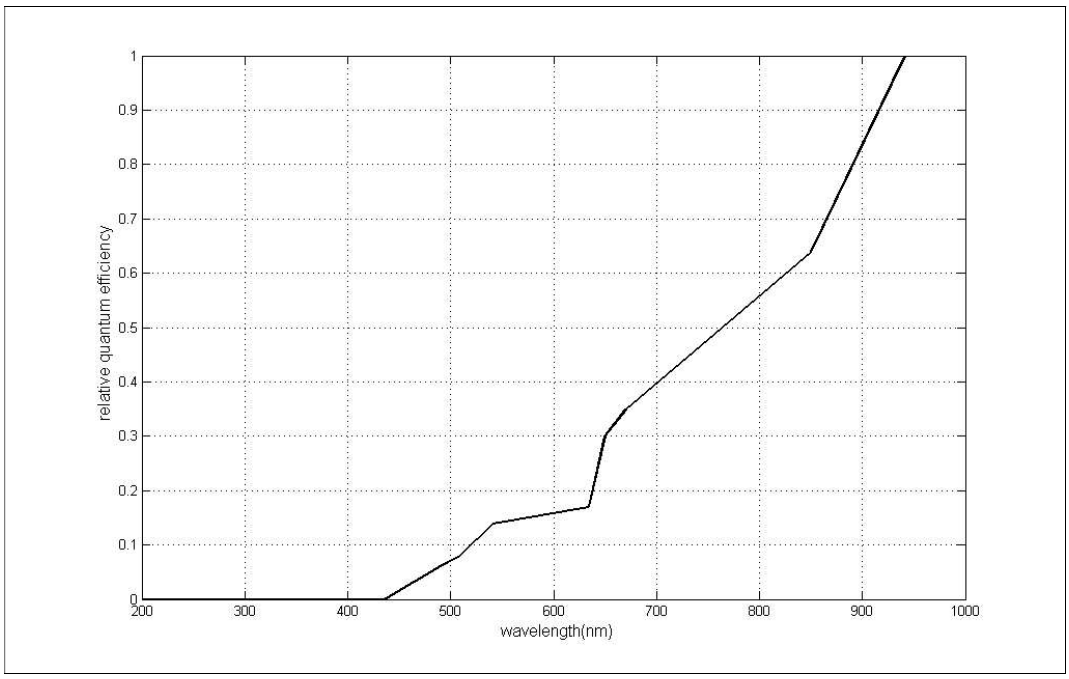

Figure (5.5): photodetector relative quantum efficiency versus wavelength

5.5 THE INDIUM-DOPED SILICON PHOTODIODE I-V CHARACTERISTICS UNDER LIGHT

Figure (5.6) shows the photogenerated current for the fabricated photodiode as a function of voltage with incident light intensity equals to 4000 lx. It is clear that the photodiode has a small open circuit voltage which is equal to 0.11 volt. The small value of the photodiode output voltage can be attributed to many reasons, the annealing process has been performed under a small value of vacuum pressure which is not enough to prevent the oxidization process and other defect during the diffusion of indium into the silicon wafer. The result is a quasi-ohmic conduction path along which leakage current flows across the junction. This is called the photodiode shunt resistance, which affects the performance of the photodiode through reduction of the fill factor. Direct electrical short may arise at pinholes or microcracks in the junction forming layer or shorts in the contact metallization around the junction.

The consideration of the IPV effect in photodiode involves a trade-off between short circuit current improvements and open circuit voltage reduction. Indium doping even under the most favorable conditions, reduces the open circuit voltage of the photodiode because of indium role as a recombination center at high operating voltages. Also both the generative and recombinative roles that the IPV impurity can play, is included in the modified SRH statistics used to calculate the generated photocurrent.

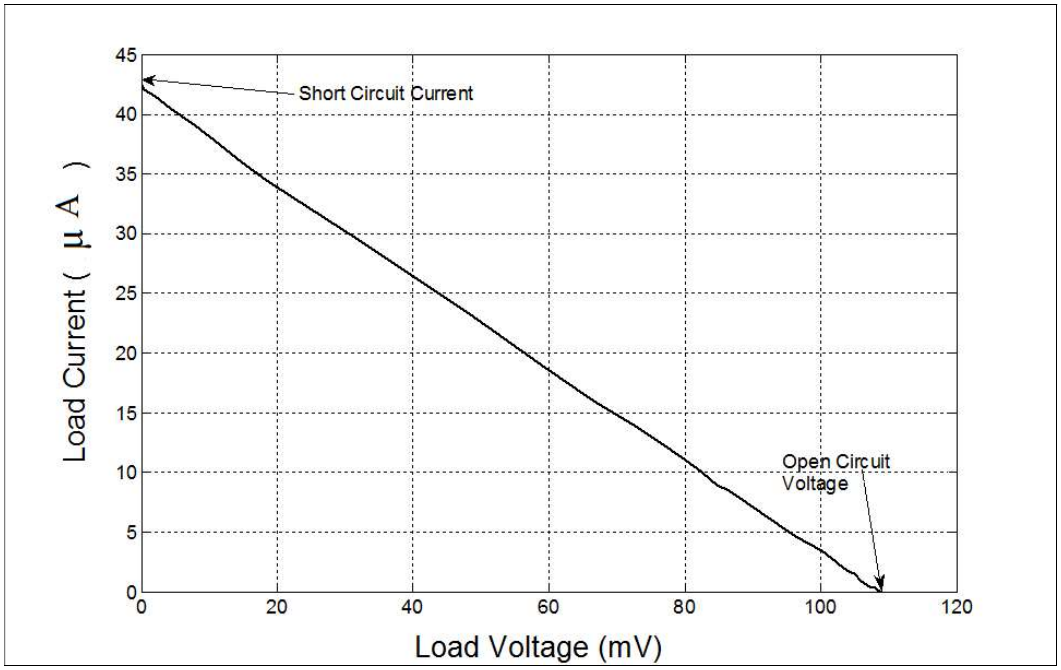

Figure (5.6): the I-V characteristics of the fabricated photodiode under light

5.6 FAILED PRACTICAL ATTEMPTS

Several attempts had been done to achieve photodiodes having better and comparative characteristics by making changes in the details of work, such as using some different methods to clean the silicon wafer and make it appropriate for use also in making the front contact for the photodiode, masks with different shapes had been used some of them are not appropriate. In addition to many attempts failed due to vacuum evaporation system unexpected problems. In the following, some discussion about these attempts.

The silicon dioxide native layer (SiO_2) makes as a capsulation layer which prevents the deposited layers from diffuse inside the silicon especially with the size of molecules of the deposited materials being larger than porous of the dioxide. Because of this, it must first

remove this oxide layer by a rigorous cleaning cycle such as a concentrated HydroFluoric acid (HF) for some seconds. In the fabrication of some samples their I-V characteristic, taken after they have been fabricated, are merely characteristics of an ordinary resistance, which means that there is no p-n junction formatted, and this is because of there is no indium diffuse in silicon, because as stated, the oxide layer is not removed because it has used a diluted HF or actually (10 H_2O , 1 HF).

The use of a dot shaped mask with a small number of dots results in a severe reduction in charge collection at the electrodes, which make the responsivity either very small or zero and in both cases the output signal could not be tracked.

Many other samples are failed because of the vacuum evaporation system unexpected problems, such as the breakdown of the boat which carries the deposited material and through which a high current passes to raise the temperature and evaporate the material, the breakdown is because of the inappropriate fixing of it in its position.

Another problem appeared is the existed materials on the walls of the chamber from previous deposition processes which will fly around when there is a high vacuum and the temperature raises inside the chamber which will result in a wrong read of the deposition rate and hence in the thickness of the deposited layer, so there must be a cleaning process to the chamber walls to remove these existed materials.

CHAPTER SIX

CONCLUSIONS AND FUTURE WORKS

6.1 CONCLUSIONS

From the simulation program results about the spectral response measurements, the following conclusions are obtained:

1. There is a spectral response of the indium-doped silicon photodiodes as the indium concentration close to compensate the background shallow dopants and continue increasing but with decreasing rate as the indium concentration exceeds the background concentration. The range of wavelengths over which most of the simulated structures are extended from about 400 to 1100 nm and this range changes slightly from one structure to another.

2. For each junction depth there is a wavelength at which maximum quantum efficiency occurs which corresponds to the wavelength at which the generated carriers are collected in the depletion region maximum than other wavelengths.

3. By changing the indium concentration, the junction depth at which the maximum quantum efficiency occurs is changing also, and as the indium concentration increases the junction depth at which the maximum quantum efficiency occurs decreases.

4. The increase of the junction depth results in decrease of the range of spectral response of the photodiode, but this will slow down the speed response of the photodiode.

5. As the n-region, wherein the generation of light is primarily because of intrinsic transition from the valence band to the conduction band, increases the quantum efficiency increases and the spectral

response will move closer toward longer wavelengths, due primarily to the impurity photovoltaic effect will enhanced.

6. As the generation-recombination centers become more efficient as recombination center, by replacing the shallow dopants by the indium, then the spectral response range will be less and move toward the longer wavelengths.

And from the practical results, the following conclusions are obtained:

1. From the I-V characteristics of the fabricated photodiode, the cut in voltage is low 0.4v and leakage current is high because of the small depletion region and the very shallow junction.

2. From the spectral response measurements of the fabricated photodiode, there is an agreement between the practical and simulated spectral response range, where the spectral response in both cases starts increasing from about 400 nm and becomes maximum at about 900 nm which indicates a good simulation process has been done.

3. Upon lightening the fabricated photodiode, the generated photovoltage is small, where the open circuit voltage is 110 mV this is because of the shunt resistance being of small value due to the fabrication conditions and also because of the recombinative role the indium impurity plays which reduces the open circuit voltage, but on the other hand the short circuit current which is 42 μA is enhanced due to the subgap absorption of the indium impurities.

6.2 FUTURE WORK

1. Fabricating photodiodes with optimum design obtained from the simulation results practically and after that a complete study of the response speed is performed to use the fabricated device as a receiving photodetectors in optical communication systems such as in remote controls.

2. Replace the indium impurity with different deep level impurities and study the spectral and speed response of the fabricated photodiode to obtain a higher speed photodiodes.

3. Study of the possibility of making a Focal Plane Arrays (FPAs) by using the indium doped silicon photodiodes.

REFERENCES

REFERENCES

[1] HAMAMATSU PHOTONICS K. K. , Solid State Division, "Characteristics and Use of Infrared Detectors", Japan 2004.

[2] UC Sharma, "Infrared Detectors", M. Tech Credit Seminar Report, Electronic Systems Group, EE Dept, IIT Bombay, 2004.

[3] Sravanthi Kache, "Optimization of Charge Collection Efficiency in MSM Photodetector", M. Sc. Thesis, University of Missouri-Columbia, 2005.

[4] Ernie L. Stelzer, Joseph L. Schmit, Obert N. Tufte, "Mercury Cadmium Telluride as an Infrared Detector Material", IEEE Transactions on Electron Devices, VOL. ED-16, NO.10, OCTOBER 1969.

[5] J. Rutkowski, "Planar Junction Formation in HgCdTe Infrared Detectors", Opto-Electronics Review 12(1), 123-128, 2004.

[6] B. Y. Tsaur, C. K. Chen, B. A. Nechay, "IrSi Schottky-Barrier Infrared Detectors with Wavelength Response Beyond 12μm", IEEE Electron Device Letters, VOL. 11, NO. 9, SEPTEMBER 1990.

[7] X. Xiao, James C. Sturm, S. R. Parihar, S. A. Lyon, D. Meyerhofer, Stephen Palfrey, F. V. Shallcross, "Silicide/Strained $Si_{1-x}Ge_x$ Schottky-Barrier Infrared Detectors", IEEE Electron Device Letters, VOL. 14, NO. 4, 1993.

[8] Waldemar Gawron, Jozef Piotrowski, "Practical Near Room-Temperature, Long-wavelength IR Photovoltaic Detectors", OPto-Electronics review, 1994.

[9] S. V. Bandara, S. D. Gunapala, J. K. Liu, S. B. Rafol, C. J. Hill, D. Z.-Y. Ting, J. M. Mumolo, T. Q. Trinh, J. M. Fastenau, A. W. K. Liu, "Tuning and tailoring of broadband quantum-well infrared photodetector responsivity spectrum", APPLIED PHYSICS LETTERS 86, 2005.

[10] N. Biyikli, I. Kimukin, T. Tut, O. Aytur, E. Ozbay, "Fabrication and characterisation of Solar-blind $Al_{0.6}Ga_{0.4}N$ MSM photodetectors", Electronics letters, Vol. 41 No. 5, 2005.

[11] H.Zogg, M. Arnold, "Narrow spectral band monolithic lead-chalcogenide-on-Si mid-IR photodetectors", Opto-Electronics review 14(1), 33-36, 2006.

[12] Xian Song Fu, Su Ying Yao, Jiang Tao Xu, Yao Lu, Yun Guang Zheng, "Study on high signal-to-noise ratio (SNR) silicon p-n junction photodetector", Optica Applicata, vol. XXXVI, No.2-3, 2006.

[13] P. Louro, Y. Vygranenko, J. Martins, M. Fernandes, M. Vieira, "Colour sensitive devices based on double p-i-n-i-p stacked photodiodes", Thin Solid Films 515, 7526–7529, 2007.

[14] Jiangbo Zhang, Ning Xi, Hongzhi Chen, King W. C. Lai, Yilun Luo, "Carbon Nanotube based Infrared Detector Array", IEEE, 2008.

[15] O. Thomas, Z. L. Yuan, J. F. Dynes, A. W. Sharpe, A. J. Shields, "Efficient photon number detection with silicon avalanche photodiodes", ARXIV, V1, 2010.

[16] Yasuhiko Ishikawa, Kazumi Wada, "Germanium for silicon photonics", Thin Solid Films 518,P.P. S83–S87, 2010.

[17] Christina F. de Souza, Azar Alizadeh, Selvakumar Nair, Igor Saveliev, Marina Blumin, Harry E. Ruda, David C. Hays, Vicki H. Watkins, Ken R. Conway, and Edit Braunstein, "Mechanism of IR Photoresponse in Nanopatterned InAs/GaAs Quantum Dot p-i-n Photodiodes", IEEE Journal OF Quantum electronics, VOL. 46, NO. 5, 2010.

[18] S. M. Sze, Kwok K. Ng, "Physics of Semiconductor Devices Third Edition", JOHN WILEY & SONS, INC., 2007.

[19] HAMAMATSU Inc., "Photodiode Technical Information", HAMAMATSU PHOTONICS K.K., Solid State Division, 2004

[20] Mark Fox, "Optical Properties of Solids", Oxford University Press, 2001.

[21] G. H. Rieke, "Detection of Light From the Ultraviolet to the Submillimeter second edition", Cambridge University Press, 2003.

[22] M. J. Keevers, M. A. Green, "Efficiency improvements of silicon solar cells by the Impurity photovoltaic effect", J. Appl. Phys. 75 (8), 15 April 1994.

[23] Khalid Khaleel Mohammed, "Fabrication and Characterization of Indium-Doped Silicon Solar Cell", M. Sc. Thesis, University of Mosul, College of Engineering, 2000.

[24] Donald A. Neamen, "Semiconductor Physics and Devices Basic Principles Third Edition", McGraw-Hill Companies Inc., 2003.

[25] M. A. Trishenkov, "Detection of Low-Level Optical Signals, Photodetectors, Focal Plane Arrays and Systems", Kluwer Academic Publishers, 1997.

[26] Nadir Dagli, "High-Speed Photonic Devices", Taylor & Francis Group, LLC, 2007.

[27] Manijeh Razeghi, "Fundamentals of Solid State Engineering", Kluwer Academic Publishers, 2002.

[28] UDT Sensors Inc., "*Photodiode Characteristics*", http:\\www.udt.com.

[29] "A New Detector for IR LED Light", as reprinted from SENSORS Magazine, December 1996 Issue.

[30] M. Burgelman, P. Nollet, S. Degrave, "Modelling polycrystalline semiconductor solar cells", Thin Solid Films, 527-532, 2000.

[31] Stefaan Degrave, Marc Burgelman, Peter Nollet, "Modelling of Polycrystalline Thin Film Solar Cells: New features in SCAPS version 2.3", WCPEC-3, Japan, 12-16 may 2003.

[32] Alex Niemegeers, Sofie Gillis, Marc Burgelman, "A user program for realistic simulation of polycrystalline heterojunction solar cells: SCAPS-1D", 2nd World Conference on Photovoltaic Energy Conversion, pp. 672-675, 1998.

[33] J. Verschraegen, M. Burgelman, "Numerical modeling of intra band tunneling for heterojunction solar cells in SCAPS", Thin Solid Films 515, 6276–6279, 2007.

[34] Marc Burgelman and Jonas Marlein, "Analysis of Graded Band Gap Solar Cells with SCAPS", 23rd European Photovoltaic Solar Energy Conference, 1-5 September 2008.

University of Mosul
College of Engineering

Study and Implementation of Infrared Photodetector Using Silicon Doped With Indium

A Thesis Submitted
By
Omar Badir Mohammad Khedir

To
The Council of the College of Engineering
University of Mosul
As a Partial Fulfillment of the Requirements
For The Degree of Master of science
In
Electrical Engineering\Electronics and communications\
(Solid State)

Supervised by
Assistant Professor
Dr. Khalid Khaleel Mohammad

2010 A.D. 1432 A.H.

University of Mosul
College of Engineering

Study and Implementation of Infrared Photodetector Using Silicon Doped With Indium

Omar Badir Mohammad Khedir

M.Sc.Thesis
Electrical Engineering/
Electronics and communications/
(Solid State)

Supervised by
Assistant Professor
Dr. Khalid Khaleel Mohammad

2010 A.D. 1432 A.H.